

# VIE Solutions of 2.5-D Electromagnetic Scattering by Arbitrary Anisotropic Objects Embedded in Layered Uniaxial Media

Feng Han<sup>ID</sup>, Senior Member, IEEE, Kemeng Tao<sup>ID</sup>, Sijia Ma<sup>ID</sup>, and Jiawen Li<sup>ID</sup>

**Abstract**—In this article, the 3-D electromagnetic (EM) scattering by 2-D dielectric arbitrary anisotropic scatterers embedded in a layered uniaxial anisotropic medium is studied. This 2.5-D EM scattering problem is mathematically formulated by the volume integral equation (VIE) whose discretized weak forms are based on the 2.5-D roof-top basis functions and solved by the stabilized biconjugate gradient fast Fourier transform (BCGS-FFT). Meanwhile, the 2.5-D dyadic Green's functions (DGFs) for the layered uniaxial media are given in detail and their evaluation is also discussed. In particular, a tricky variable replacement strategy is proposed to obtain analytical expressions for partial 2.5-D DGF components. Besides the validation of the 2.5-D DGPs by comparing them with the corresponding 3-D values, several numerical experiments are also carried out to validate the accuracy and efficiency of the BCGS-FFT solver for the 2.5-D EM scattering in the layered anisotropic circumstance by comparing the results with those obtained by a 3-D VIE solver. The major new contribution of this work is to extend the 2.5-D EM scattering computation to accommodate the uniaxial anisotropy of the layered background medium and the arbitrary anisotropic scatterers.

**Index Terms**—2.5-D, arbitrary anisotropic scatterers, electromagnetic (EM) scattering, layered uniaxial media.

## I. INTRODUCTION

LECTROMAGNETIC (EM) scattering refers to the phenomenon that an object embedded inside the background medium will generate a fictitious current under the action of an external EM wave, thereby radiating a scattered EM field. Since EM scattering has an increasingly wide range of applications such as microwave imaging [1], geophysical exploration [2], remote sensing [3], land mine detection [4], and subsurface unexploded ordnance sensing [5], it is of great practical significance to investigate the mechanism of scattering as well as the efficient evaluation of scattered fields.

Usually, in some simple EM scattering scenarios, analytical solutions can be obtained. For example, in [6], for the first

Received 4 September 2024; revised 29 January 2025; accepted 18 February 2025. This work was supported by the National Natural Science Foundation of China under Grant 62271428. (Corresponding author: Feng Han.)

Feng Han, Kemeng Tao, and Sijia Ma are with the School of Computing and Information Technology, Great Bay University, Dongguan, Guangdong 523000, China, and also with the Institute of Electromagnetics and Acoustics, Xiamen University, Xiamen 361005, China (e-mail: feng.han@gbu.edu.cn; feng.han@xmu.edu.cn).

Jiawen Li is with the School of Electronic and Information Engineering, Guangxi Normal University, Guilin, Guangxi 541004, China (e-mail: jiawenli@mailbox.gxnu.edu.cn).

Digital Object Identifier 10.1109/TAP.2025.3547922

time, Mie gave the analytically mathematical derivation for the scattering of an EM plane wave by a sphere with arbitrary size and any electric properties placed in a homogeneous background medium. This Mie theory was later extended to EM scattering by a sphere immersed in an absorbing background medium [7], by coated spheres [8], and by anisotropic dielectric spheres [9]. Unfortunately, these analytical solutions are only valid for scatterers with regular shapes placed in ideal background media. For objects with arbitrary shapes embedded in a layered or anisotropic medium, it is necessary to adopt some numerical methods to solve their EM scattering. One of the commonly used numerical methods is using the integral equation. For highly conductive or uniform homogeneous scatterers, the surface integral equation (SIE) is preferred [10], [11]. However, for inhomogeneous dielectric scatterers, the volume integral equation (VIE) is always adopted [12], [13].

In the early days, the SIEs and VIEs were discretized and directly solved by the method of moments (MoMs) [14], [15]. Nevertheless, for scatterers with large electrical sizes, the computational cost of MoM is usually unaffordable [16]. Several modified numerical methods have been proposed to improve the MoM and save both the memory consumption and central processing unit (CPU) time. They can be roughly categorized into two types. The first type is based on an iterative scheme that usually utilizes the fast Fourier transform (FFT) to accelerate the convolution integrals. For example, the conjugate gradient FFT (CG-FFT) transforms the cumbersome integration into simple algebraic multiplication in the spectral domain [17], [18], [19]. As a result, the CPU time in each iteration is lowered to the order of  $N \log N$  compared to  $N^3$  in MoM, where  $N$  is the total knowns in the computational domain. Meanwhile, the storage requirement is reduced by CG-FFT from  $O(N^2)$  to  $O(N)$ . Gan and Chew later proposed the biconjugate gradient (BCG) method that avoids the singularity problem due to Green's function and the limitation of the sampling rate of FFT [20]. Numerical simulation shows that BCG-FFT is around three–six times faster than the CG-FFT for a typical EM scattering case [21]. The stabilized BCGS-FFT [22], [23] is another FFT-based method that converges faster than CG-FFT and smoother than BCG-FFT and thus is suitable for solving large-scale EM scattering problems. The second type of modification to the MoM is based on approximating the far-zone interactions. Typical methods include the fast multipole algorithm (FMA), adaptive

integral method (AIM), and precorrected-FFT (pFFT). In the implementation of the FMA [24], [25], the discretized meshes in the computational domain are first spatially clustered into several groups. Then, the addition theorem is used to translate the scattered fields from different meshes in the same group into one from its center. Finally, for each group, the scattered field caused by all the other group centers is first received by the group center, and then it is redistributed to all the meshes belonging to this group. The FMA was later further developed into the multilevel FMA (MLFMA) [26] in which the aforementioned three steps are carried out at different levels. The AIM accelerates the solution of an integral equation by decomposing the MoM matrix into a near-field part that is sparse and a far-field part whose multiplication with a vector can be accelerated by FFT [27]. The pFFT [28] is similar to the AIM since it also treats differently the near- and far-field interactions when evaluating the matrix–vector multiplication. However, it has a mesh spacing larger than that of the AIM [29]. These fast algorithms have been successfully applied to the computation of EM scattering for 2-D isotropic magnetodielectric objects embedded in layered isotropic media [30], 3-D isotropic objects embedded in layered media [23], 3-D anisotropic magnetodielectric objects placed in free space [31], embedded in homogeneous uniaxial media [32], and in layered uniaxial media [33], and 3-D arbitrary anisotropic objects embedded in layered arbitrary anisotropic media [34]. Finally, it is worth mentioning that, besides these aforementioned iterative methods, some direct solvers that explicitly compute the inverse of the impedance matrix can effectively overcome the ill-conditioned systems without using preconditioners [35]. As a result, they also have been adopted to 3-D EM problems, for example, nanoantenna radiation [36] and negative permittivity material scattering [35].

In computational EMs, in addition to 2-D and 3-D problems, there is another important class of scattering problems, namely, the 2.5-D scattering in which the EM fields with three components are generated by 3-D sources and the medium is heterogeneous only in two directions, for example, the  $xz$ -plane but maintains invariant in the perpendicular  $\hat{y}$ -direction. Therefore, the EM field is treated in a full-vector 3-D manner but the computational domain is restricted to a 2-D region located in the  $xz$ -plane. This 2.5-D EM scattering has important applications in geophysical exploration such as computing the responses of underground conductive bodies in controlled-source EM (CSEM) and magnetotelluric (MT) surveys [37] based on finite-element method (FEM) since many 3-D geological conductive bodies are generally elongated in a strike direction and thus their physical properties can be approximately considered unchanged in that direction and only show variations in its orthogonal 2-D plane [38]. Similarly, in the coal mine excavation, the underground water-bearing structure detection by transient EM (TEM) method has been accomplished by 2.5-D finite-difference time domain (FDTD) [39]. On the other hand, VIEs also have been successfully employed to solve 2.5-D EM scattering problems. For example, in [40], the VIE was used to solve 2.5-D low-frequency response to almost infinitely long geological bodies. Besides, in the high-frequency EM scattering applications, the 2.5-D

VIE has been applied to the computation of 3-D millimeter-wave scattering by large inhomogeneous 2-D objects [41], [42]. However, in most of these existing works based on integral equations, the stratification and anisotropy of the media are not taken into account.

Therefore, in this article, for the first time, we address the 2.5-D EM scattering problem for dielectric arbitrary anisotropic scatterers embedded in a layered uniaxial anisotropic background medium based on VIEs. That is, we assume that the principal axis of the background medium is perpendicular to the layer interface, but that of the scatterer can be rotated in any direction. Starting from the integral equation, we make full use of the characteristics of the 2.5-D structure and combine 2.5-D roof-top basis functions, 2.5-D dyadic Green's functions (DGFs) in layered uniaxial anisotropic media, the Legendre–Gauss quadrature approximation for numerical integration, and the BCGS-FFT solver to realize the calculation of the 2.5-D EM scattering. After that, we carry out some numerical experiments to verify the correctness of 2.5-D DGFs and the computational accuracy and efficiency of the 2.5-D BCGS-FFT solver by comparing the obtained results with some 3-D BCGS-FFT computation results.

The organization of this article is as follows. In Section II, the method used in this article and the related formula derivation are described in detail. This section is mainly composed of four parts, including 2.5-D roof-top basis functions, electric field VIEs, 2.5-D DGFs in layered uniaxial anisotropic media, and the derived weak forms. In Section III, several numerical examples are given to validate the proposed method. Finally, the conclusion is drawn in Section IV.

## II. FORMULATION

In this section, we solve the 2.5-D EM scattering by arbitrary anisotropic objects embedded in a layered uniaxial medium. Related mathematical formulas and derivations are given in the framework of VIEs. As shown in Fig. 1, both the 2-D background medium and the 2-D scatterers located in the  $m$ th layer are invariant in the  $\hat{y}$ -direction and illuminated by 3-D EM waves excited by 3-D transmitters. Since we only consider the nonmagnetic material with its permeability the same as free space  $\mu_0$ , the relative permittivity and conductivity tensors of the  $i$ th layer of the background medium are written as

$$\bar{\epsilon}_b^i = \begin{bmatrix} \epsilon_{11}^b & 0 & 0 \\ 0 & \epsilon_{22}^b & 0 \\ 0 & 0 & \epsilon_{33}^b \end{bmatrix}, \quad \bar{\sigma}_b^i = \begin{bmatrix} \sigma_{11}^b & 0 & 0 \\ 0 & \sigma_{22}^b & 0 \\ 0 & 0 & \sigma_{33}^b \end{bmatrix} \quad (1)$$

where  $\epsilon_{11}^b = \epsilon_{22}^b$  and  $\sigma_{11}^b = \sigma_{22}^b$  are for the uniaxial background medium. The superscript  $b$  denotes the background. The relative complex permittivity of the  $i$ th layer is written as

$$\bar{\epsilon}_b^i = \bar{\epsilon}_b^i + \frac{\bar{\sigma}_b^i}{j\omega\epsilon_0} \quad (2)$$

where  $\omega$  refers to the angular frequency of the EM wave. Similarly, the relative permittivity and conductivity tensors of

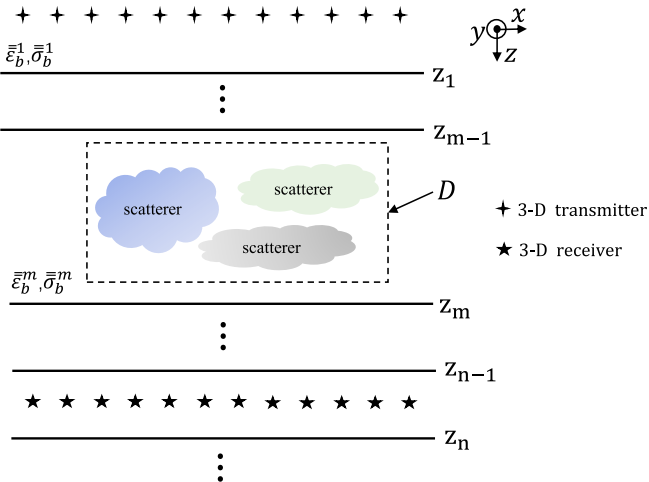


Fig. 1. Configuration of 2.5-D EM scattering by arbitrary anisotropic scatterers embedded in a layered uniaxial anisotropic medium.

the nonmagnetic anisotropic scatterer placed in any layer can be written as

$$\bar{\epsilon}_s = \begin{bmatrix} \epsilon_{11}^s & \epsilon_{12}^s & \epsilon_{13}^s \\ \epsilon_{21}^s & \epsilon_{22}^s & \epsilon_{23}^s \\ \epsilon_{31}^s & \epsilon_{32}^s & \epsilon_{33}^s \end{bmatrix}, \quad \bar{\sigma}_s = \begin{bmatrix} \sigma_{11}^s & \sigma_{12}^s & \sigma_{13}^s \\ \sigma_{21}^s & \sigma_{22}^s & \sigma_{23}^s \\ \sigma_{31}^s & \sigma_{32}^s & \sigma_{33}^s \end{bmatrix} \quad (3)$$

where  $s$  denotes the scatterer. Besides, the complex relative permittivity tensor of the scatterer can be written as

$$\bar{\epsilon}_s = \bar{\epsilon}_b + \frac{\bar{\sigma}_s}{j\omega\epsilon_0}. \quad (4)$$

#### A. 2.5-D Roof-Top Basis Functions

Since the integral equations must be discretized and solved numerically, we first introduce the 2.5-D roof-top basis functions. Because the EM fields are only expanded in the  $xz$ -plane, the 2.5-D basis function  $\Psi_i^{(q)}$  is similar to the 2-D one and has a different mathematical form from the 3-D basis function [18]. It is written as

$$\psi_i^{(1)}(x, z) = \Lambda\left(x - x_i + \frac{1}{2}\Delta x; 2\Delta x\right)\Pi(z - z_i; \Delta z) \quad (5a)$$

$$\psi_i^{(2)}(x, z) = \Pi(x - x_i; \Delta x)\Pi(z - z_i; \Delta z) \quad (5b)$$

$$\psi_i^{(3)}(x, z) = \Pi(x - x_i; \Delta x)\Lambda\left(z - z_i + \frac{1}{2}\Delta z; 2\Delta z\right) \quad (5c)$$

where  $q = 1, 2, 3$  are corresponding to  $x, y, z$  three components, respectively, and  $i = \{I, K\}$  are the indices of the discretized pixels in the  $\hat{x}$ - and  $\hat{z}$ -directions. Similarly, for the testing function, it is denoted by  $\Psi_m^{(p)}$  with  $p = 1, 2, 3$  and  $m = \{M, P\}$  which are also the indices of the discretized pixels in the  $\hat{x}$ - and  $\hat{z}$ -directions. Since we adopt the Galerkin method,  $\Psi_m^{(p)}$  has the same mathematical expression as  $\Psi_i^{(q)}$ . It is worth noting that, in (5),  $\Lambda(x - a; b)$  is the 1-D piecewise linear and continuous function, viz. the triangle function with the support  $b$  and the central axis  $a$ , and  $\Pi(x - c; d)$  is the 1-D piecewise constant function, viz. the pulse function with the support  $d$  and the central axis  $c$ .  $x_i$  and  $z_i$  are the coordinates of the center points of each discrete pixel in the  $\hat{x}$ - and  $\hat{z}$ -directions, respectively.

#### B. 2.5-D Electric Field VIE

Since the media are invariant in the  $\hat{y}$ -direction and thus the EM field components are spatially smooth, we can implement the forward and inverse spatial Fourier transforms in the  $\hat{y}$ -direction to shift between the spatial-domain  $\mathbf{E}(\rho, y)$  and the spectral-domain  $\tilde{\mathbf{E}}(\rho, k_y)$  with

$$\tilde{\mathbf{E}}(\rho, k_y) = \mathcal{F}_{1Dy}\{\mathbf{E}(\rho, y)\} \quad (6a)$$

$$\mathbf{E}(\rho, y) = \mathcal{F}_{1Dy}^{-1}\{\tilde{\mathbf{E}}(\rho, k_y)\} \quad (6b)$$

where  $\rho = x\hat{x} + z\hat{z}$  represents the spatial position in the  $xz$ -plane and the definitions of  $\mathcal{F}_{1Dy}$  and  $\mathcal{F}_{1Dy}^{-1}$  are given in Appendix A. Similarly, we apply  $\mathcal{F}_{1Dy}$  to [33], eqs. (7) and (8), invoke the property of Fourier transform of convolution, and obtain the spectral-domain

$$\tilde{\mathbf{E}}_{sct}^n(\rho, k_y) = -j\omega\left(1 + \frac{1}{k_0^2\epsilon_{11}^b}\tilde{\nabla}\tilde{\nabla}\cdot\right)\tilde{\mathbf{A}}^n(\rho, k_y) \quad (7)$$

and

$$\tilde{\mathbf{A}}^n(\rho, k_y) = j\omega\mu_0\int_D \tilde{\mathbf{G}}_A^{nm}(\rho, \rho', k_y) \cdot \bar{\chi}(\rho')\tilde{\mathbf{D}}_{tot}^m(\rho', k_y)d\rho' \quad (8)$$

where

$$\tilde{\nabla} = \hat{x}\frac{\partial}{\partial x} - \hat{y}jk_y + \hat{z}\frac{\partial}{\partial z} \quad (9)$$

is the 2.5-D Nabla operator and

$$\bar{\chi}(\rho) = [\bar{\epsilon}(\rho) - \bar{\epsilon}_b]\bar{\epsilon}^{-1}(\rho) \quad (10)$$

is the anisotropic electric contrast of the scatterer located in the  $m$ th layer and inside the  $xz$ -plane.  $\tilde{\mathbf{G}}_A^{nm}$  is the layered 2.5-D DGF which represents the magnetic vector potential in the  $n$ th layer generated by a unit electric dipole source with an arbitrary direction and located in the  $m$ th layer. Its computation will be discussed in Section II-C. The  $D$  is the 2-D computation domain wrapping scatterers and located inside the  $xz$ -plane, as shown in Fig. 1. Then, the spectral-domain 2.5-D electric field integral equation (EFIE) in layered media is formulated as

$$\begin{aligned} \tilde{\mathbf{E}}_{inc}^n(\rho, k_y) &= \tilde{\mathbf{E}}_{tot}^n(\rho, k_y) - \tilde{\mathbf{E}}_{sct}^n(\rho, k_y) \\ &= \bar{\epsilon}^{-1}(\rho)\frac{\tilde{\mathbf{D}}_{tot}^n(\rho, k_y)}{\epsilon_0} - \left(\omega^2\mu_0 + \frac{1}{\epsilon_0\epsilon_{11}^b}\tilde{\nabla}\tilde{\nabla}\cdot\right) \\ &\quad \times \int_D \tilde{\mathbf{G}}_A^{nm}(\rho, \rho', k_y) \cdot \bar{\chi}(\rho')\tilde{\mathbf{D}}_{tot}^m(\rho', k_y)d\rho' \end{aligned} \quad (11)$$

where  $\tilde{\mathbf{D}}_{tot} = \epsilon_0\bar{\epsilon}\tilde{\mathbf{E}}_{tot}$  is the total electric flux density.  $\tilde{\mathbf{E}}_{inc}$ ,  $\tilde{\mathbf{E}}_{tot}$ , and  $\tilde{\mathbf{E}}_{sct}$  represent the incident, total, and scattered electrical fields in the  $n$ th layer. In the forward scattering computation, we always let  $n$  be equal to  $m$  and compute  $\tilde{\mathbf{E}}_{tot}$  in the  $m$ th layer.

Once  $\tilde{\mathbf{D}}_{tot}$  is obtained, the following data equation is used to compute the scattered electric field at the receiver array located in the  $n$ th layer

$$\tilde{\mathbf{E}}_{sct}^n(\rho, k_y) = j\omega\int_D \tilde{\mathbf{G}}_{EJ}^{nm}(\rho, \rho', k_y) \cdot \bar{\chi}(\rho')\tilde{\mathbf{D}}_{tot}^m(\rho', k_y)d\rho' \quad (12a)$$

$$\tilde{\mathbf{H}}_{sct}^n(\rho, k_y) = j\omega \int_D \tilde{\mathbf{G}}_{\mathbf{HJ}}^{nm}(\rho, \rho', k_y) \cdot \bar{\chi}(\rho') \tilde{\mathbf{D}}_{tot}^m d\rho' \quad (12b)$$

where  $\tilde{\mathbf{G}}_{\mathbf{EJ}}^{nm}$  and  $\tilde{\mathbf{G}}_{\mathbf{HJ}}^{nm}$  are the layered 2.5-D DGFs connecting the equivalent current source in the  $m$ th layer and the scattered fields in the  $n$ th layer and their computation will be discussed in Section II-C. All the above computation is performed in the  $xz$ -plane for a certain  $k_y$  value. The spatial-domain electric fields can be obtained via (6b) and it is numerically implemented through Legendre–Gauss quadrature integration [43]. It is worth mentioning here that the spatial-domain  $\mathbf{E}_{tot}$  is only evaluated in the  $y = 0$   $xz$ -plane while  $\mathbf{E}_{sct}$  is recorded in any spatial position.

### C. 2.5-D DGFs in Layered Uniaxial Anisotropic Media

The 2.5-D DGFs in layered uniaxial media are contributed by two parts, the primary fields and the transmission and reflection in layer boundaries. The evaluation of the primary fields starts from isotropic media and is extended to uniaxial anisotropic media. The detailed procedure will be displayed in the following. Computation of the layer boundary transmission and reflection follows a similar procedure as the Sommerfeld integral discussed in [44]. The major difference is that the inverse spatial Fourier transforms of [44, eqs. (28)–(31) and (41)] are only performed with respect to  $k_x$  instead of to both  $k_x$  and  $k_y$ .

We first assume both the transmitter and the receiver are placed inside a homogeneous isotropic medium having the wavenumber  $k$  and compute the primary field parts of the 2.5-D DGFs. The spatial Fourier transform given in (A1) is applied to the 3-D scalar Green's function to obtain the 2.5-D scalar Green's function [45]

$$\tilde{g} = \mathcal{F}_{1Dy}\{g\} = -\frac{j}{4} H_0^{(2)}(k_\rho \rho) \quad (13)$$

where  $k_\rho = (k^2 - k_y^2)^{1/2}$  and  $H_0^{(2)}$  is the zeroth-order Hankel function of the second kind. The scalar  $g$  in (13) is computed using

$$g(\mathbf{r}, \mathbf{r}') = \frac{\exp(-jk|\mathbf{r} - \mathbf{r}'|)}{4\pi |\mathbf{r} - \mathbf{r}'|}. \quad (14)$$

Because the 3-D spatial-domain DGFs in a homogeneous isotropic medium are evaluated by

$$\bar{\mathbf{G}}_{\mathbf{A}} = \mu \cdot \text{diag}\{g, g, g\} \quad (15a)$$

$$\bar{\mathbf{G}}_{\mathbf{EJ}} = -j\omega\mu\mu_0 \left( \bar{\mathbf{I}} + \frac{\nabla\nabla}{k^2} \right) g \quad (15b)$$

$$\bar{\mathbf{G}}_{\mathbf{HJ}} = \nabla \times \text{diag}\{g, g, g\} \quad (15c)$$

we apply  $\mathcal{F}_{1Dy}$  to both sides of (15) and substitute  $\tilde{g}$  in (13) as well as  $\bar{\nabla}$  in (9) into the transformed (15) and come to the 2.5-D  $\bar{\mathbf{G}}_{\mathbf{A}}$ ,  $\bar{\mathbf{G}}_{\mathbf{EJ}}$ , and  $\bar{\mathbf{G}}_{\mathbf{HJ}}$  in a homogeneous isotropic medium. Their detailed components are listed in Appendix B.

When the homogeneous background medium becomes uniaxial anisotropic, the diagonal elements of  $\bar{\mathbf{G}}_{\mathbf{A}}$  can be obtained using [46, eq. 21] and [44, eqs. (42), (43), and (62)] based on the identity of [47] and a variable replacement method which will be discussed later. Unfortunately, the  $\hat{z}\hat{x}$ - and

$\hat{z}\hat{y}$ -components can only be numerically evaluated by applying (A2b) to the primary field parts of the spectral-domain DGFs (in both  $\hat{x}$ - and  $\hat{y}$ -directions) given in [46, eq. (21)] and [44, eq. (45)]. The results are listed in Appendix C.

In addition, it is noted that the 2.5-D  $\tilde{\mathbf{G}}_{\mathbf{EJ}}$  and  $\tilde{\mathbf{G}}_{\mathbf{HJ}}$  listed in Appendix B are derived using (A1a). On the other hand, they can also be obtained by applying (A2b) to the primary field parts of the spectral-domain DGFs given in [46, eq. (21)] and [44, eqs. (28)–(31)]. Let us take  $\tilde{G}_{EJ}^{xz}$  as an example and have

$$\begin{aligned} \tilde{G}_{EJ}^{xz} &= \mathcal{F}_{1Dx}^{-1} \left( \pm \frac{1}{2} \frac{k_x}{\omega\epsilon_0} \exp[-jk_z|z - z'|] \right) \\ &= \pm \frac{-j}{2\pi\omega\epsilon_0} \int_0^{+\infty} k_x \exp[-jk_z|z - z'|] \sin[k_x(x - x')] dk_x \\ &= -\frac{\omega\mu\mu_0}{4} \cdot \frac{k_\rho^2}{k^2} \cdot \frac{(x - x')(z - z')}{\rho^2} \cdot H_2^{(2)}(k_\rho\rho) \end{aligned} \quad (16)$$

where  $k_z = (k^2 - k_x^2 - k_y^2)^{1/2}$  and the odd or even property of the integrand with respect to  $k_x$  is invoked. Now, if the homogeneous medium is uniaxial anisotropic, by also applying the 1-D inverse Fourier transform, we have

$$\begin{aligned} \mathcal{F}_{1Dx}^{-1} &\left( \pm \frac{1}{2} \frac{k_x}{\omega\epsilon_{33}\epsilon_0} \exp[-jk_z^e|z - z'|] \right) \\ &= \pm \frac{-j}{2\pi\omega\epsilon_{33}\epsilon_0} \int_0^{+\infty} k_x \exp[-jk_z^e|z - z'|] \sin[k_x(x - x')] dk_x \end{aligned} \quad (17)$$

where  $k_z^e = (k^2 - v^e k_x^2 - v^e k_y^2)^{1/2}$  and  $k = \sqrt{\epsilon_{11}\mu_{11}}k_0$ . Note  $v^e = \epsilon_{11}/\epsilon_{33}$  is the electric anisotropy ratio of the background medium and  $\mu_{11}$  is one in our work. By using variable replacements with  $k'_x = \sqrt{v^e}k_x$ ,  $k'_y = \sqrt{v^e}k_y$ ,  $k_x = (k'_x/\sqrt{v^e})$ ,  $k_y = (k'_y/\sqrt{v^e})$ , and  $k'_z = (k^2 - k'^2_x - k'^2_y)^{1/2}$ , the right-hand side of (17) becomes

$$\pm \frac{-j}{2\pi\omega\epsilon_{33}\epsilon_0 v^e} \int_0^{+\infty} k'_x \exp[-jk'_z|z - z'|] \sin \left[ k'_x \frac{(x - x')}{\sqrt{v^e}} \right] dk'_x. \quad (18)$$

By comparing (16) with (18), we obtain the closed-form  $\tilde{G}_{EJ}^{xz}$  in an uniaxial anisotropic medium

$$\tilde{G}_{EJ}^{xz} = -\frac{\omega\mu_{11}\mu_0}{4} \cdot \frac{k_{\rho_e}^2}{k^2} \cdot \frac{(x - x')(z - z')}{\sqrt{v^e}\rho_e^2} \cdot H_2^{(2)}(k_{\rho_e}\rho_e) \quad (19)$$

where  $\rho_e = (((x - x')^2/v^e) + (z - z')^2)^{1/2}$  and  $k_{\rho_e} = (k^2 - v^e k_y^2)^{1/2}$ .

Note the above variable replacement strategy stretching the wave numbers  $k_x$ ,  $k_y$ , and  $k_z$  using anisotropy ratio can only be applied to any component of the primary field part of the spectral-domain  $\tilde{\mathbf{G}}_{\mathbf{EJ}}$  or  $\tilde{\mathbf{G}}_{\mathbf{HJ}}$  given in [46, eq. (21)] and [44, eqs. (28)–(31)] which has one term. If it includes two terms added together, for example,  $\tilde{G}_{EJ}^{xx}$ , the variable replacement strategy fails because  $v^e$  and  $v^h$  may be different. Here,  $v^h = \mu_{11}/\mu_{33}$  is the magnetic anisotropy ratio of the background medium. In this situation, the 2.5-D DGF must be computed by applying (A2b) to  $\tilde{\mathbf{G}}_{\mathbf{EJ}}$  and  $\tilde{\mathbf{G}}_{\mathbf{HJ}}$ . The detailed components of the 2.5-D  $\tilde{\mathbf{G}}_{\mathbf{EJ}}$  and  $\tilde{\mathbf{G}}_{\mathbf{HJ}}$  in a homogeneous uniaxial medium are listed in Appendix C.

356 *D. Discretization and Weak Forms*

357 Since (11) is a continuous integral equation, we must  
 358 linearize and discretize it before solving it. We use the 2.5-D  
 359 roof-top basis functions described in Section II-A and expand  
 360 the total electric flux density, the incident electric field, and  
 361 the magnetic vector potential, respectively, into the following  
 362 forms:

$$\tilde{D}_{tot}^{n(q)}(\rho, k_y) = \varepsilon_0 \sum_{\mathbf{i}} d_{\mathbf{i}}^{(q)} \psi_{\mathbf{i}}^{(q)}(\rho) \quad (20a)$$

$$\tilde{E}_{inc}^{n(q)}(\rho, k_y) = \sum_{\mathbf{i}} E_{\mathbf{i}}^{i,(q)} \psi_{\mathbf{i}}^{(q)}(\rho) \quad (20b)$$

$$\tilde{A}^{n(q)}(\rho, k_y) = \sum_{\mathbf{i}} A_{\mathbf{i}}^{(q)} \psi_{\mathbf{i}}^{(q)}(\rho) \quad (20c)$$

363 in which  $q = 1, 2, 3$  are corresponding to  $x, y, z$  three  
 364 components, respectively, and  $\mathbf{i} = \{I, K\}$  are the indices of the  
 365 discretized pixels in  $\hat{x}$ - and  $\hat{z}$ -directions, respectively. We then  
 366 use the same roof-top function  $\Psi_{\mathbf{m}}^{(p)}$  to test both sides of the  
 367 EFIE (11) and the preliminary weak form is obtained as

$$e_{\mathbf{m}}^{i,(p)} = \sum_{\mathbf{i}} \sum_{q=1}^3 d_{\mathbf{i}}^{(q)} u_{\mathbf{m};\mathbf{i}}^{(p,q)} + A_{\mathbf{i}}^{(q)} \left[ j\omega v_{\mathbf{m};\mathbf{i}}^{(p,q)} - \frac{j}{\omega\varepsilon_0\mu_0\epsilon_{11}^b} w_{\mathbf{m};\mathbf{i}}^{(p,q)} \right] \quad (21)$$

373 where

$$u_{\mathbf{m};\mathbf{i}}^{(p,q)} = \delta_{p,q} \int_D \psi_{\mathbf{m}}^{(p)}(\rho) \bar{\epsilon}^{-1}(\rho) \psi_{\mathbf{i}}^{(q)}(\rho) d\rho \quad (22a)$$

$$v_{\mathbf{m};\mathbf{i}}^{(p,q)} = \delta_{p,q} \int_D \psi_{\mathbf{m}}^{(p)}(\rho) \psi_{\mathbf{i}}^{(q)}(\rho) d\rho \quad (22b)$$

$$w_{\mathbf{m};\mathbf{i}}^{(p,q)} = \int_D \partial_p \psi_{\mathbf{m}}^{(p)}(\rho) \partial_q \psi_{\mathbf{i}}^{(q)}(\rho) d\rho \quad (22c)$$

377 and

$$e_{\mathbf{m}}^{i,(p)} = \sum_{\mathbf{i}} \sum_{q=1}^3 E_{\mathbf{i}}^{i,(q)} v_{\mathbf{m};\mathbf{i}}^{(p,q)} \quad (23a)$$

$$\mathbf{A}_{\mathbf{i}} = j\omega\varepsilon_0\mu_0\Delta s \cdot \sum_{\mathbf{i}'} \tilde{\mathbf{G}}_{\mathbf{A}}(\mathbf{i}, \mathbf{i}') \cdot (\bar{\chi}_{\mathbf{i}'} \cdot \mathbf{d}_{\mathbf{i}'}) \quad (23b)$$

380 In (20)–(23),  $\delta_{p,q}$  is the Kronecker symbol,  $A_{\mathbf{i}}^{(q)}$  is one  
 381 component of the magnetic vector potential  $\mathbf{A}_{\mathbf{i}}$ ,  $\mathbf{i} = \{I, K\}$  are  
 382 indices for field point pixels, while  $\mathbf{i}' = \{I', K'\}$  are indices for  
 383 equivalent current pixels,  $\Delta s = \Delta x \Delta z$  is the discretized pixel  
 384 area, and  $\mathbf{d}_{\mathbf{i}'}$  is a vector containing  $d_{I',K'}^{(q)}$  with  $q = 1, 2, 3$ .

385 Based on the expressions of the roof-top basis function  $\Psi_{\mathbf{i}}^{(q)}$   
 386 and testing function  $\Psi_{\mathbf{m}}^{(p)}$  given in (5), it is not difficult to  
 387 perform the integrals in  $u_{\mathbf{m}}^{(p,q)}$ ,  $v_{\mathbf{m}}^{(p,q)}$ , and  $w_{\mathbf{m}}^{(p,q)}$  in (21).  
 388 In this way, we obtain the final weak form of (21) as

$$e_{\mathbf{m}}^{i,(p=1)} = \sum_{q=1}^3 \sum_{l=1}^3 \mathbf{S}_{\mathbf{m},l}^{(p=1,q)} \left[ d_{\mathbf{m}+\hat{x}_p(l-2)}^{(q)} + \delta_{q,3} d_{\mathbf{m}+\hat{x}_p(l-2)+\hat{x}_q}^{(q)} \right] + \sum_{l=1}^3 \mathbf{Q}_l^{(p=1,q=1)} A_{\mathbf{m}+\hat{x}_p(l-2)}^{(p=1)} + \sum_{q=2,3}^2 \sum_{i=1}^2 \mathbf{T}_{ij}^{(p=1,q)} A_{\mathbf{m}+\hat{x}_p(i-2)+\hat{x}_q(j-1)}^{(q)} \quad (24a)$$

$$e_{\mathbf{m}}^{i,(p=2)} = \sum_{q=1,3}^3 \sum_{l=1}^3 \mathbf{S}_{\mathbf{m},l}^{(p=2,q)} d_{\mathbf{m}+\hat{x}_q(l-2)}^{(q)} + \sum_{l=1}^3 \mathbf{S}_{\mathbf{m},l}^{(p=2,q=2)} d_{\mathbf{m}}^{(q=2)} + \sum_{l=1}^3 \mathbf{Q}_l^{(p=2,q=2)} A_{\mathbf{m}}^{(p=2)} \quad (24b)$$

$$+ \sum_{q=1,3}^3 \sum_{i=1}^2 \mathbf{T}_{ij}^{(p=2,q)} A_{\mathbf{m}+\hat{x}_p(i-2)+\hat{x}_q(j-1)}^{(q)} \quad (24b)$$

$$e_{\mathbf{m}}^{i,(p=3)} = \sum_{q=1}^3 \sum_{l=1}^3 \mathbf{S}_{\mathbf{m},l}^{(p=3,q)} \left[ d_{\mathbf{m}+\hat{x}_p(l-2)}^{(q)} + \delta_{q,1} d_{\mathbf{m}+\hat{x}_p(l-2)+\hat{x}_q}^{(q)} \right] + \sum_{l=1}^3 \mathbf{Q}_l^{(p=3,q=3)} A_{\mathbf{m}+\hat{x}_p(l-2)}^{(p=3)} + \sum_{q=1,2}^2 \sum_{i=1}^2 \mathbf{T}_{ij}^{(p=3,q)} A_{\mathbf{m}+\hat{x}_p(i-2)+\hat{x}_q(j-1)}^{(q)} \quad (24c)$$

$$+ \sum_{q=1,2}^2 \sum_{i=1}^2 \mathbf{T}_{ij}^{(p=3,q)} A_{\mathbf{m}+\hat{x}_p(i-2)+\hat{x}_q(j-1)}^{(q)} \quad (24c)$$

$$+ \sum_{q=1,2}^2 \sum_{i=1}^2 \mathbf{T}_{ij}^{(p=3,q)} A_{\mathbf{m}+\hat{x}_p(i-2)+\hat{x}_q(j-1)}^{(q)} \quad (24c)$$

$$+ \sum_{q=1,2}^2 \sum_{i=1}^2 \mathbf{T}_{ij}^{(p=3,q)} A_{\mathbf{m}+\hat{x}_p(i-2)+\hat{x}_q(j-1)}^{(q)} \quad (24c)$$

where  $T$  is the matrix transpose and  $\hat{x}_p$  and  $\hat{x}_q$  are the unit vectors in the  $p$ th and  $q$ th directions, respectively.  $\mathbf{S}_{\mathbf{m}}^{(p,q)}$  is the  $l$ th component of the vector  $\mathbf{S}_{\mathbf{m}}^{(p,q)}$  whose expression is

$$\mathbf{S}_{\mathbf{m}}^{(p,q)} = \begin{cases} \frac{\Delta s}{6} \left[ \bar{\epsilon}_{\mathbf{m}-\hat{x}_p,pp}^{-1} 2\bar{\epsilon}_{\mathbf{m}-\hat{x}_p,pp}^{-1} + 2\bar{\epsilon}_{\mathbf{m},pp}^{-1} \bar{\epsilon}_{\mathbf{m},pp}^{-1} \right]^T, & p=q=1 \text{ or } 3 \\ \frac{\Delta s}{3} \left[ \bar{\epsilon}_{\mathbf{m},pp}^{-1} \bar{\epsilon}_{\mathbf{m},pp}^{-1} \bar{\epsilon}_{\mathbf{m},pp}^{-1} \right]^T, & p=q=2 \\ \frac{\Delta s}{2} \left[ 0 \bar{\epsilon}_{\mathbf{m},pq}^{-1} \bar{\epsilon}_{\mathbf{m},pq}^{-1} \right]^T, & p=2, q=1 \text{ or } p=2, q=3 \\ \frac{\Delta s}{4} \left[ \bar{\epsilon}_{\mathbf{m}-\hat{x}_p,pq}^{-1} \bar{\epsilon}_{\mathbf{m},pq}^{-1} 0 \right]^T, & p=1, q=3 \text{ or } p=3, q=1 \\ \frac{\Delta s}{2} \left[ \bar{\epsilon}_{\mathbf{m}-\hat{x}_p,pq}^{-1} \bar{\epsilon}_{\mathbf{m},pq}^{-1} 0 \right]^T, & p=1, q=2 \text{ or } p=3, q=2 \end{cases} \quad (25)$$

where  $\bar{\epsilon}_{pq}^{-1}$  is the  $pq$ th component of the full tensor  $\bar{\epsilon}^{-1}$ .  $\mathbf{Q}_l^{(p,q)}$  is the  $l$ th component of the vector  $\mathbf{Q}^{(p,q)}$  whose expression is

$$\mathbf{Q}^{(p,q)} = \begin{cases} \Delta s \left\{ \frac{j\omega}{6} [1 \ 4 \ 1]^T - \frac{j[-1 \ 2 \ -1]^T}{\omega\mu_0\varepsilon_0\epsilon_{11}^b(\Delta x_p)^2} \right\}, & p=q=1 \text{ or } 3 \\ \Delta s \left\{ \frac{j\omega}{3} [1 \ 1 \ 1]^T - \frac{j k_y^2 [1 \ 1 \ 1]^T}{3\omega\mu_0\varepsilon_0\epsilon_{11}^b} \right\}, & p=q=2 \end{cases} \quad (26)$$

where  $\Delta x_{p=1} = \Delta x$  and  $\Delta x_{p=3} = \Delta z$ .  $\mathbf{T}_{ij}^{(p,q)}$  is the  $(ij)$ th component of the  $2 \times 2$  matrix  $\mathbf{T}^{(p,q)}$  whose expression is

$$\mathbf{T}^{(p,q)} = \begin{cases} -\frac{\Delta s k_y}{\omega\mu_0\varepsilon_0\epsilon_{11}^b\Delta x_p} \begin{bmatrix} 1 & 0 \\ -1 & 0 \end{bmatrix}, & p=1 \text{ or } 3, q=2 \\ -\frac{j}{\omega\mu_0\varepsilon_0\epsilon_{11}^b} \begin{bmatrix} -1 & 1 \\ 1 & -1 \end{bmatrix}, & p=1, q=3 \text{ or } p=3, q=1 \\ -\frac{\Delta s k_y}{\omega\mu_0\varepsilon_0\epsilon_{11}^b\Delta x_q} \begin{bmatrix} 0 & 0 \\ 1 & -1 \end{bmatrix}, & p=2, q=1 \text{ or } 3. \end{cases} \quad (27)$$

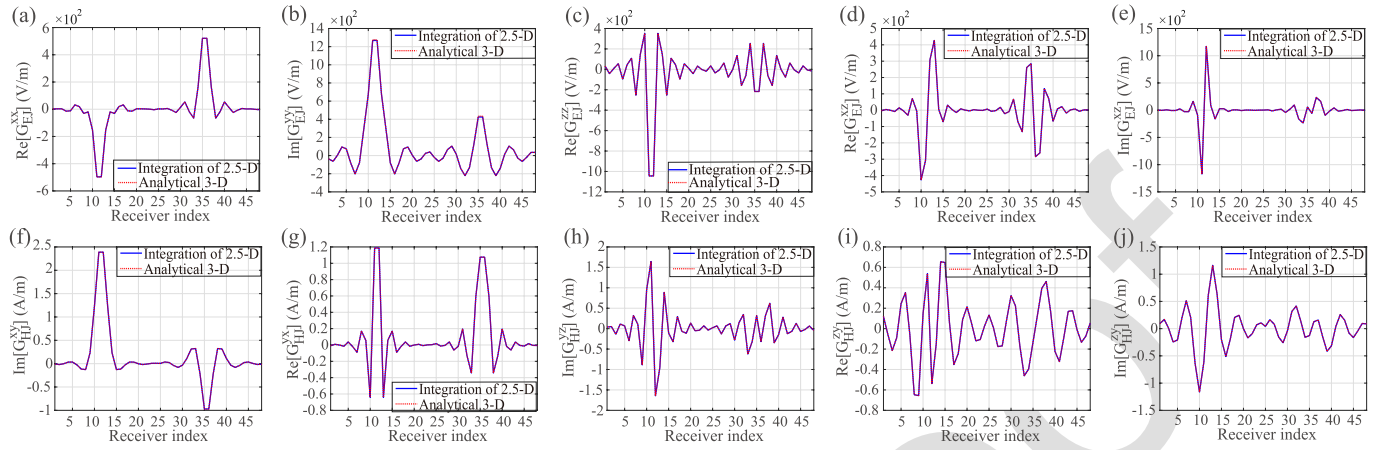


Fig. 2. Comparisons of the numerical integration of 2.5-D results and analytical 3-D solutions for (a) real part of  $G_{EJ}^{XX}$ , (b) imaginary part of  $G_{EJ}^{YY}$ , (c) real part of  $G_{EJ}^{ZZ}$ , (d) real part of  $G_{EJ}^{XZ}$ , (e) imaginary part of  $G_{EJ}^{XZ}$ , (f) imaginary part of  $G_{HJ}^{XY}$ , (g) real part of  $G_{HJ}^{YX}$ , (h) imaginary part of  $G_{HJ}^{YZ}$ , (i) real part of  $G_{HJ}^{ZY}$ , and (j) imaginary part of  $G_{HJ}^{ZY}$ .

413 In the forward scattering computation, the coefficients  $d^{(q)}$   
 414 in (24) are solved for by BCGS-FFT [33]. Since the layered  
 415 medium DGFs can be decomposed into the “minus” and  
 416 “plus” parts [12] in the vertical  $\hat{z}$ -direction, the integration  
 417 of the multiplication between  $\tilde{\mathbf{G}}_A$  and the equivalent current  
 418  $\tilde{\mathbf{X}}_{\mathbf{i}' \cdot \mathbf{d}_{\mathbf{i}'}}$  in (23b) can be converted into discrete convolution  
 419 in the horizontal  $\hat{x}$ -direction and discrete convolution plus  
 420 correlation in the vertical  $\hat{z}$ -direction, respectively. Therefore,  
 421 the summation computation in (23) can be accelerated by  
 422 FFT. Details of the implementation of BCGS-FFT can be  
 423 found in our previous work [33] in which its efficiency is also  
 424 discussed.

### 425 III. NUMERICAL RESULTS

426 In this section, we use three numerical cases to verify  
 427 the derived formulas and results presented in Section II.  
 428 In the first case, we validate the correctness of the derived  
 429 primary parts of 2.5-D DGFs in a uniaxial medium given in  
 430 Appendix C by applying Fourier transform in the  $\hat{y}$ -direction  
 431 to them and compare the numerical integration results with  
 432 the analytical solutions of 3-D DGFs given in the appendix  
 433 of [32]. In the second case, we validate the correctness of  
 434 the EFIE solutions for 2.5-D EM scattering from arbitrary  
 435 anisotropic scatterers embedded in a planarly layered uniaxial  
 436 medium. We first solve the incident fields in the computational  
 437 domain and at the receiver array. Then, we solve the weak  
 438 forms (24) by BCGS-FFT and obtain the total electrical fields  
 439 in the computational domain. Finally, the scattered fields at  
 440 the receiver array are computed by using (12). These 2.5-D  
 441 incident fields, total fields, and scattered fields are validated  
 442 by comparing them with the corresponding 3-D results [33]  
 443 when the anisotropic scatterer is almost infinitely long in  
 444 the  $\hat{y}$ -direction. In the last case, we build an airborne EM  
 445 (AEM) survey model to compare the time and memory con-  
 446 sumption of 2.5-D and 3-D EM scattering computation in  
 447 the circumstance of layered uniaxial media. All the numerical  
 448 experiments are performed on a workstation with an 18-core  
 449 Intel i9-10980XE 3.00 GHz CPU and 256 GB RAM.

#### A. Case 1: Validation of 2.5-D DGFs in a Homogeneous Uniaxial Medium

The purpose of this case is to verify the correctness of the derived  $\tilde{\mathbf{G}}_{EJ}$  and  $\tilde{\mathbf{G}}_{HJ}$  given in Appendix C. One should note that the derivation of 2.5-D DGFs in this article is also applicable to media having permeability uniaxial anisotropy although the 2.5-D EM scattering solved by the EFIE only accounts for permittivity uniaxial anisotropy. Therefore, for the validation of 2.5-D DGFs, the permeability uniaxial anisotropy is included. It is assumed that the homogeneous uniaxial anisotropic medium has the parameters  $\bar{\epsilon} = \text{diag}\{1, 1, 1.5\}$ ,  $\bar{\sigma} = \text{diag}\{2, 2, 3\}$  mS/m, and  $\bar{\mu} = \text{diag}\{2, 2, 1\}$ . The operation frequency is 300 MHz. There is only one transmitter located at the origin. Totally,  $24 \times 2$  receivers are located in the  $y = 0$   $xz$ -plane. The first receiver has the position coordinate  $(x_r, z_r) = (-2.1, -0.2)$  m. The interval between two adjacent receivers in the  $\hat{x}$ -direction is 0.2 m, while it is 0.6 m in the  $\hat{z}$ -direction. The last receiver has the position coordinate  $(x_r, z_r) = (2.5, 0.4)$  m. As shown in Fig. 2, ten representative components of the DGFs computed by the integration of 2.5-D results and those by the 3-D analytical method given in the Appendix of [32] match well. Other components also have the same good fit and are not shown here due to space limitations. The mean relative error between the integration of 2.5-D results and the 3-D analytical solution is 0.15%.

#### B. Case 2: An Inhomogeneous Arbitrary Anisotropic Scatterer Embedded in a Three-Layer Uniaxial Medium

As shown in Fig. 3, the background medium includes three layers. The top layer is free space. The middle layer is uniaxial anisotropic with the dielectric parameters  $\bar{\epsilon}_b = \text{diag}\{2.0, 2.0, 3.0\}$ ,  $\bar{\sigma}_b = \text{diag}\{1.0, 1.0, 1.5\}$  mS/m, and  $\bar{\mu}_b = \text{diag}\{1.0, 1.0, 1.0\}$ . The bottom layer is also uniaxial anisotropic but with the dielectric parameters  $\bar{\epsilon}_b^3 = \text{diag}\{1.5, 1.5, 1.0\}$ ,  $\bar{\sigma}_b^3 = \text{diag}\{3.0, 3.0, 2.0\}$  mS/m, and  $\bar{\mu}_b^3 = \text{diag}\{1.0, 1.0, 1.0\}$ . Two-layer boundaries are located at  $z = -0.4$  m and  $z = 0.4$  m, respectively.

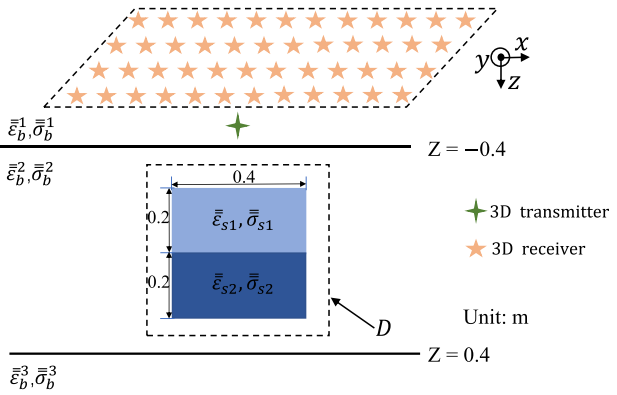


Fig. 3. Configuration of a two-layer arbitrary anisotropic square scatterer with the dimensions of  $0.4 \times 0.4$  m embedded in a three-layer uniaxial anisotropic background medium.

The inhomogeneous scatterer placed in the second layer has the dimensions of  $0.4 \times 0.4$  m and its center is located at  $z = 0$ . It includes two subscatterers. The dielectric parameters of the top subscatterer are initially set as  $\bar{\epsilon}_{s1} = \text{diag}\{4.0, 3.0, 2.0\}$ ,  $\bar{\sigma}_{s1} = \text{diag}\{2.0, 4.0, 6.0\}$  mS/m, and  $\bar{\mu}_{s1} = \text{diag}\{1.0, 1.0, 1.0\}$ . Correspondingly, the parameters of the bottom subscatterer are initially set as  $\bar{\epsilon}_{s2} = \text{diag}\{2.0, 3.0, 4.0\}$ ,  $\bar{\sigma}_{s2} = \text{diag}\{5.0, 4.0, 3.0\}$  mS/m, and  $\bar{\mu}_{s2} = \text{diag}\{1.0, 1.0, 1.0\}$ . We then follow the procedure given in [48, eqs. (1)–(3)] and rotate the principal axes of two subscatterers to form the arbitrary anisotropic parameters. The rotation angles are  $\phi_1 = 30^\circ$  and  $\phi_2 = 60^\circ$  for the top subscatterer. They are  $\phi_1 = 60^\circ$  and  $\phi_2 = 120^\circ$  for the bottom one. The final relative permittivity and conductivity values of the scatterer used in the computation are as follows:

$$\bar{\epsilon}'_{s1} = \begin{bmatrix} 3.063 & -0.541 & -0.375 \\ -0.541 & 3.688 & -0.217 \\ -0.375 & -0.217 & 2.25 \end{bmatrix} \quad (28a)$$

$$\bar{\sigma}'_{s1} = \begin{bmatrix} 3.875 & 1.083 & 0.75 \\ 1.083 & 2.625 & 0.433 \\ 0.75 & 0.433 & 5.5 \end{bmatrix} \text{ mS/m} \quad (28b)$$

$$\bar{\epsilon}'_{s2} = \begin{bmatrix} 3.313 & -0.758 & 0.375 \\ -0.758 & 2.438 & -0.217 \\ -0.375 & -0.217 & 3.25 \end{bmatrix} \quad (28c)$$

$$\bar{\sigma}'_{s2} = \begin{bmatrix} 3.688 & 0.758 & -0.375 \\ 0.758 & 4.562 & 0.217 \\ -0.375 & 0.217 & 3.75 \end{bmatrix} \text{ mS/m.} \quad (28d)$$

The computational domain  $D$  enclosing the scatterer has the dimensions of  $0.5 \times 0.5$  m and is discretized into  $50 \times 50$  pixels in the  $xz$ -plane. The size of each square pixel is  $0.01 \times 0.01$  m. There is only one transmitter located at  $(x_s, y_s, z_s) = (0.0, 0.0, -0.5)$  m. It is a unit electric dipole operated at 800 MHz and polarized by  $(1, 1, 1)$ . The  $12 \times 4$  receiver array is located at the  $z = -0.65$  m  $xy$ -plane. The increment interval between two adjacent receivers in the  $\hat{x}$ -direction is 0.1 m but 0.2 m in the  $\hat{y}$ -direction. The coordinate of the first receiver is  $(x_r, y_r, z_r) = (-0.55, -0.3, -0.65)$  m. To verify the correctness of the derived 2.5-D formulas in Section II, we compare the computed EM fields to those evaluated based on the 3-D

formulas in [33]. The  $xz$  cross section of the adopted 3-D model is exactly the same as the 2.5-D model shown in Fig. 3. However, its layered background medium is extended to infinite in the  $\hat{y}$ -direction. Meanwhile, the two-layer anisotropic scatterer is stretched to more than  $37\lambda_0$  in the  $\hat{y}$ -direction. Here,  $\lambda_0$  is the wavelength in free space.

First, let us validate the incident fields in the computational domain  $D$  and at the receiver array when the scatterer is absent. We compare the integration of 2.5-D  $\tilde{\mathbf{E}}_{inc}$  and the 3-D  $\mathbf{E}_{inc}$  obtained via the formulas shown in [33]. There are totally  $7 \times 7$  sampling points located inside the computational domain  $D$  at the  $y = 0$   $xz$ -plane. The uniform increment intervals of these points are 0.08 m in both the  $\hat{x}$ - and  $\hat{z}$ -directions. The first sampling point is located at  $(-0.24, -0.24)$  m. Fig. 4 shows the comparisons of incident fields in the computational domain and at the receiver array. Due to space limitations, only partial components are presented. We can see that the obtained incident fields from the 2.5 model and the 3-D model in the computational domain  $D$  and at the receiver array match well. Other components not shown in Fig. 4 have similar good matches. The relative errors of  $E_{inc}^x$ ,  $E_{inc}^y$ , and  $E_{inc}^z$  from the 2.5-D model with respect to those from the 3-D model when they are sampled inside the domain  $D$  are 0.00005%, 0.0024%, and 0.008%, respectively. When the electric fields are sampled at the receiver array, these relative errors are 0.00002%, 0.0002%, and 0.002%, respectively. On the other hand, the relative errors of  $H_{inc}^x$ ,  $H_{inc}^y$ , and  $H_{inc}^z$  from the 2.5-D model with respect to those from the 3-D model when they are sampled at the receiver array are 0.000015%, 0.0%, and 0.0%, respectively. These low errors confirm the correctness of the computation of the 2.5-D incident fields when the transmitter and the receivers are located inside the same layer or in different layers.

Then, let us validate the total electric fields in the computational domain  $D$  when the scatterer is present by comparing the integration of 2.5-D  $\tilde{\mathbf{E}}_{tot}$  solved from the weak forms in (24) and the 3-D  $\mathbf{E}_{tot}$  obtained via [33, eq. (27)]. They are sampled in the same positions mentioned above in which the incident fields are sampled. The comparisons of the three components between the integration of 2.5-D results and the 3-D results are shown in Fig. 5. We can see that all three components have good matches. The relative errors of  $E_{tot}^x$ ,  $E_{tot}^y$ , and  $E_{tot}^z$  from the 2.5-D model with respect to those from the 3-D model are 0.12%, 0.10%, and 0.25%, respectively. These low values justified the correctness of the derived weak forms in (24).

Finally, the correctness of the 2.5-D  $\tilde{\mathbf{E}}_{sct}$  at the  $12 \times 4$  receiver array is confirmed by comparing their integration values in (12) to the 3-D values obtained via [33, eq. (9)]. Fig. 6 shows the comparisons of five representative components of the scattered fields.  $H_{sct}^z$  is not shown here due to the space limitation. However, it also has similar good matches as those illustrated in Fig. 6(a)–(j). The relative errors of  $E_{sct}^x$ ,  $E_{sct}^y$ , and  $E_{sct}^z$  from the 2.5-D model with respect to those from the 3-D model are 0.62%, 0.16%, and 1.0%, respectively. The corresponding errors for  $H_{sct}^x$ ,  $H_{sct}^y$ , and  $H_{sct}^z$  are 0.20%, 0.058%, and 0.13%, respectively. Obviously, the 2.5-D model proposed in this work also can compute the scattered fields reliably.

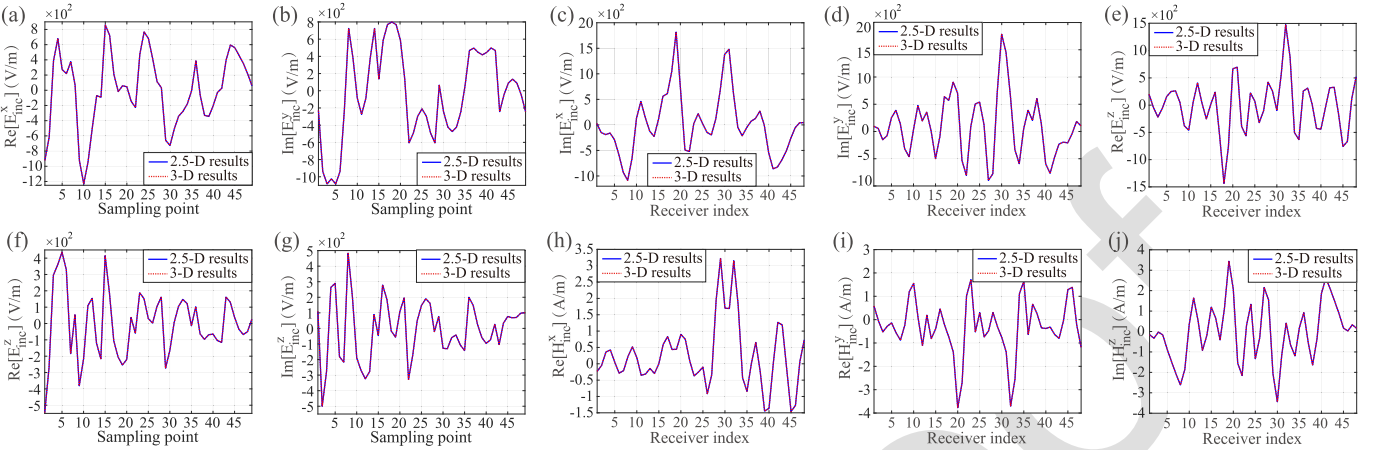


Fig. 4. Comparisons of the incident fields from the 2.5-D computational model and those from the 3-D computational model for (a) real part of  $E_{inc}^x$  in the domain  $D$ , (b) imaginary part of  $E_{inc}^y$  in the domain  $D$ , (c) imaginary part of  $E_{inc}^x$  at the receiver array, (d) imaginary part of  $E_{inc}^y$  at the receiver array, (e) real part of  $E_{inc}^z$  at the receiver array, (f) real part of  $E_{inc}^z$  in the domain  $D$ , (g) imaginary part of  $E_{inc}^y$  in the domain  $D$ , (h) real part of  $H_{inc}^x$  at the receiver array, (i) real part of  $H_{inc}^y$  at the receiver array, and (j) imaginary part of  $H_{inc}^z$  at the receiver array.

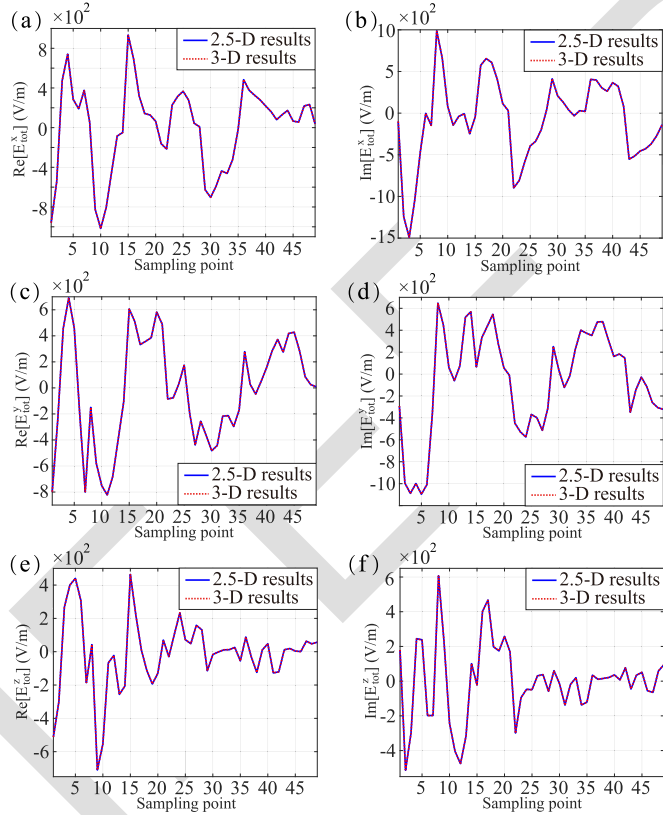


Fig. 5. Comparisons of the total electric fields from the 2.5-D computational model and those from the 3-D computational model inside the domain  $D$  for (a) real part of  $E_{tot}^x$ , (b) imaginary part of  $E_{tot}^x$ , (c) real part of  $E_{tot}^y$ , (d) imaginary part of  $E_{tot}^y$ , (e) real part of  $E_{tot}^z$ , and (f) imaginary part of  $E_{tot}^z$ .

### C. Case 3: An AEM Survey to Detect Underground Anisotropic Circular Cylinders

To demonstrate the superiority of a 2.5-D model over a 3-D model in computing EM scattering from scatterers having long invariance in a certain direction, we simulate a frequency-domain AEM survey to detect two concentric

anisotropic circular cylinders buried underground. As shown in Fig. 7, the common center of two cylinders is located at (50.0, 50.0) m. Their geometry sizes are annotated in the figure. The computational domain  $D$  wrapping the cylinders has the size of 80 × 80 m and is discretized into 40 × 40 pixels. The transmitter coil operated at 50 kHz is treated as a vertical magnetic dipole with the unit intensity and is located at  $(x_s, y_s, z_s) = (0.0, 0.0, -50.0)$  m. The scattered vertical magnetic field  $H_{sct}^z$  is observed in a uniform 7 × 7 horizontal array located at the  $z_r = -50$  m plane. The first observation point has the coordinate  $(x_r, y_r, z_r) = (-300.0, -300.0, -50.0)$  m. The increment intervals of these observation points are 100 m in both the  $\hat{x}$ - and  $\hat{y}$ -directions. The underground region beneath the  $z = 0.0$  plane is uniaxially anisotropic and its conductivity is  $\bar{\sigma}_b^2 = \text{diag}\{1.0, 1.0, 2.0\}$  mS/m. The two concentric cylinders are arbitrarily anisotropic. The initial conductivity of the inner one is  $\bar{\sigma}_{s1} = \text{diag}\{8.0, 10.0, 15.0\}$  mS/m, while that of the outer one is  $\bar{\sigma}_{s2} = \text{diag}\{10.0, 6.0, 18.0\}$  mS/m. We then rotate the principal axis of the inner cylinder with  $\phi_1 = 60^\circ$  and  $\phi_2 = 150^\circ$ , rotate that of the outer cylinder with  $\phi_1 = 120^\circ$  and  $\phi_2 = 45^\circ$ , recompute the arbitrarily anisotropic parameters based on [48, eqs. (1)–(3)], and come to

$$\bar{\sigma}'_{s1} = \begin{bmatrix} 9.438 & -2.490 & 1.082 \\ -2.490 & 12.31 & -1.875 \\ 1.082 & -1.875 & 11.25 \end{bmatrix} \text{ mS/m} \quad (29a)$$

$$\bar{\sigma}'_{s2} = \begin{bmatrix} 12.50 & 2.50 & -3.674 \\ 2.50 & 12.50 & -3.674 \\ -3.674 & -3.674 & 9.0 \end{bmatrix} \text{ mS/m.} \quad (29b)$$

Finally, one should note that the two concentric cylinders have a length of 8 km in the 3-D model which is long enough to imitate an infinite length. The whole domain is discretized into  $40 \times 4000 \times 40$  voxels in the 3-D EM scattering computation. The 2.5-D  $\tilde{\mathbf{G}}_{\text{EM}}$  used to compute the incident fields inside the domain  $D$  is obtained via applying the duality theorem to  $\tilde{\mathbf{G}}_{\text{HJ}}$  given in Appendix C.

Fig. 8 shows the comparisons of the scattered  $H_{sct}^z$  at 49 observation points computed by the 2.5-D EM scatter-

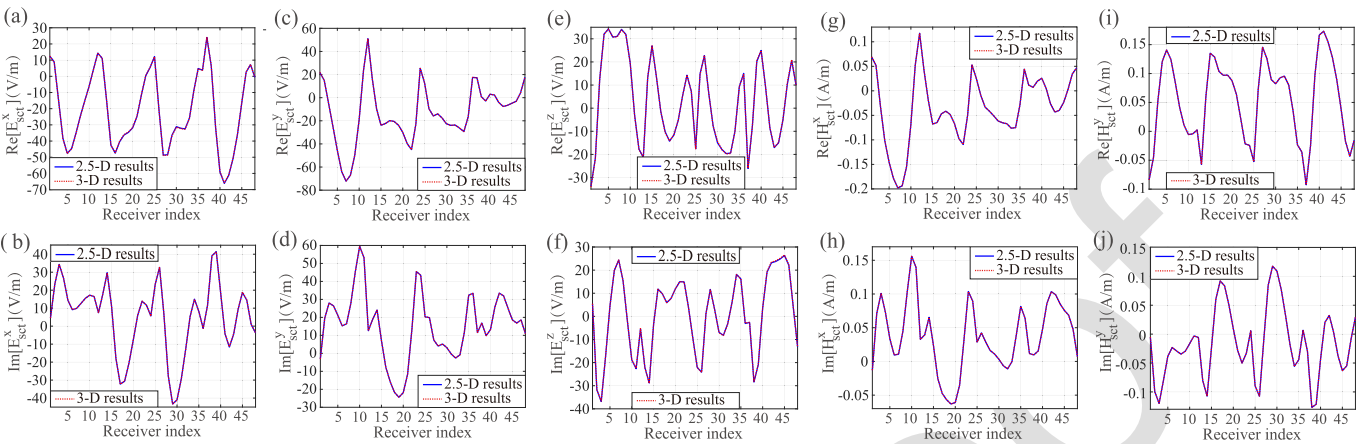


Fig. 6. Comparisons of the scattered fields from the 2.5-D computational model and those from the 3-D computational model sampled at the receiver array for (a) real part of  $E_{sct}^x$ , (b) imaginary part of  $E_{sct}^x$ , (c) real part of  $E_{sct}^y$ , (d) imaginary part of  $E_{sct}^y$ , (e) real part of  $E_{sct}^z$ , (f) imaginary part of  $E_{sct}^z$ , (g) real part of  $H_{sct}^x$ , (h) imaginary part of  $H_{sct}^x$ , (i) real part of  $H_{sct}^y$ , and (j) imaginary part of  $H_{sct}^y$ .

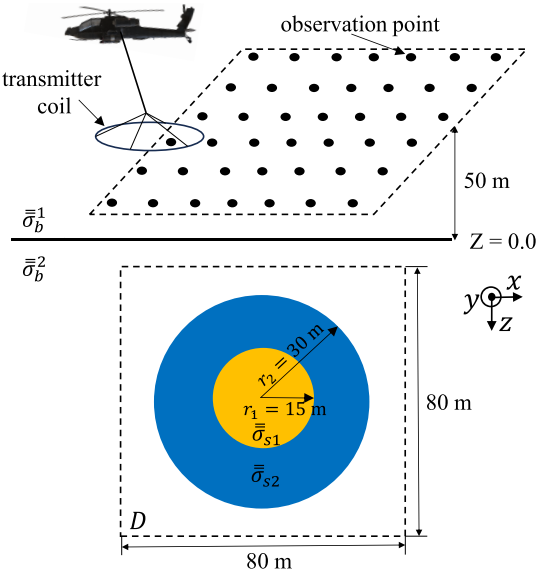


Fig. 7. Configuration of an AEM survey model with two infinitely long concentric anisotropic cylinders buried in the underground region. The geometry parameters of the two cylinders and the computational domain  $D$  are annotated in the figure.

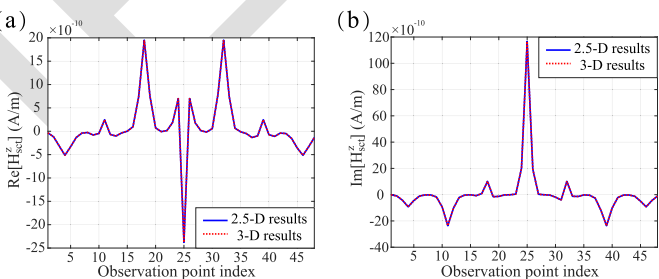


Fig. 8. Comparisons of the vertical scattered magnetic fields from the 2.5-D computational model and those from the 3-D computational model sampled at different observation points for (a) real part of  $H_{sct}^z$  and (b) imaginary part of  $H_{sct}^z$ .

TABLE I  
COMPARISON OF COMPUTATION CONFIGURATION AND COST IN CASE 3

	CPU	total time	BCGS time	$k_y$	integral points	memory
3-D model	16C/32T	1069 s	165 s	N/A		23.1 GB
2.5-D model	16C/32T	80 s	0.44×3×2 s	32×3×2		0.07 GB

Remark: The 16C/32T means 16 cores with 32 threads.

bodies. Table I lists the computation configuration and cost of the 3-D model and our 2.5-D model for this simulated AEM survey. We can see that, with almost the same parallel computing using 16 CPU cores/32 threads, both the computation time and memory cost of our 2.5-D model are less than 10% of those consumed by the 3-D model. There are two major reasons for this big discrepancy. The first one is the implementation of BCGS to solve for the total electric fields inside the computational domain. In the 3-D EM scattering computation, the BCGS-FFT iterations only can be implemented sequentially. By contrast, in the 2.5-D model, the BCGS iterations can be directly parallelized for different  $k_y$  values. Note in our 2.5-D model, the 32-point Legendre-Gauss quadrature is adopted and thus the computation of incident, total, and scattered fields for 32 different  $k_y$  values are independently implemented in 32 threads. The whole integration path for  $k_y$  is uniformly divided into a series of segments. The 32-point Legendre-Gauss quadrature is implemented in each segment. The length of each segment is determined based on the Nyquist sampling theorem to guarantee there are at least two Legendre-Gauss points in each spatial period of the inverse Fourier transform. The  $\times 3$  in the fourth and fifth columns of Table I means the integration for  $k_y$  in the inverse Fourier transform converges in three steps. The  $\times 2$  means the integration is performed symmetrically for both  $k_y$  and  $-k_y$ . As listed in the 4th column of Table I, the BCGS in the 2.5-D model in each thread only needs 0.44 s. The total time of 2.64 s is significantly less than the 3-D BCGS time. The second reason lies in the computation of the scattered fields. The 3-D model must compute the scattered fields at all observation points since the layered DGFs for different observation points are different. By contrast, in the

ing model and the 3-D model [33]. The relative error is 0.025%. This good match indicates the reliability of our 2.5-D model for computing EM scattering from large geology

2.5-D model, the DGFs are the same as long as the  $x_r$  and  $z_r$  coordinates of the observation points are the same. The  $y_r$  coordinate does not affect the evaluation of DGFs. Its influence is manifested in the inverse Fourier transform to compute the spatial-domain scattered fields. Therefore, in the aforementioned AEM survey, our 2.5-D model actually only computes spectral-domain  $H_{sct}^z$  for the first seven observation points having the same  $y_r$  coordinate. This of course will significantly save the computation time.

#### IV. SUMMARY AND CONCLUSION

In this article, a VIE-based 2.5-D numerical model to compute the EM scattering from 2-D arbitrary anisotropic inhomogeneous scatterers embedded in layered uniaxial media and illuminated by 3-D sources was developed. The 2.5-D EFIE was derived by implementing the Fourier transform in the  $\hat{y}$ -direction to the 3-D EFIE given [33]. The evaluation of the 2.5-D DGFs which is most important to the accurate solution of the 2.5-D EFIE was also discussed in detail. It was found that partial components of the primary-field parts of 2.5-D DGFs for a uniaxial medium have analytical expressions that are obtained via variable replacement. Other components can only be computed via inverse Fourier transform in the  $\hat{x}$ -direction. However, all components of the 2.5-D DGFs accounting for layer boundary reflection and transmission must be evaluated via exerting the  $\hat{x}$ -direction inverse Fourier transform to the spectral-domain DGFs given in [44]. Finally, the weak forms for the 2.5-D EFIE were also derived based on 2.5-D rooftop basis functions and were ready for iteratively solving.

Three numerical experiments were performed to justify the correctness of the obtained 2.5-D DGFs in layered uniaxial media, the solutions of the 2.5-D state equation and data equation, and the computation efficiency of the 2.5-D model by comparing their integration results in the  $\hat{y}$ -direction with the corresponding results computed by the 3-D model given in [33] and [44]. It is found that the proposed 2.5-D model in this work can obtain the same incident fields, total fields, and scattered fields as those obtained by the 3-D model given in [33] but with a much lower cost. The high efficiency of our 2.5-D model is because the solution in the  $\hat{y}$ -direction is in the spectral domain instead of in the spatial domain and the implementation can be directly parallelized.

#### APPENDIX A

The 1-D forward and inverse spatial Fourier transforms in the  $\hat{y}$ -direction are defined as follows:

$$\tilde{f}(x, k_y, z) = \mathcal{F}_{1Dy}\{f(x, y, z)\} = \int_{-\infty}^{+\infty} f \cdot \exp\{jk_y y\} dy \quad (\text{A1a})$$

$$f(x, y, z) = \mathcal{F}_{1Dy}^{-1}\{\tilde{f}(x, k_y, z)\} = \frac{1}{2\pi} \int_{-\infty}^{+\infty} \tilde{f} \cdot \exp\{-jk_y y\} dk_y. \quad (\text{A1b})$$

The 1-D forward and inverse spatial Fourier transforms in the  $\hat{x}$ -direction are defined as follows:

$$\tilde{f}(k_x, k_y, z) = \mathcal{F}_{1Dx}\{\tilde{f}(x, k_y, z)\}$$

$$= \int_{-\infty}^{+\infty} \tilde{f} \cdot \exp\{jk_x x\} dx \quad (\text{A2a})$$

$$\begin{aligned} \tilde{f}(x, k_y, z) &= \mathcal{F}_{1Dx}^{-1}\{\tilde{f}(k_x, k_y, z)\} \\ &= \frac{1}{2\pi} \int_{-\infty}^{+\infty} \tilde{f} \cdot \exp\{-jk_x x\} dk_x. \end{aligned} \quad (\text{A2b})$$

One should note that  $x$ ,  $y$ , and  $z$  in (A1) and (A2) should be replaced with  $x - x'$ ,  $y - y'$ , and  $z - z'$ , respectively, if the source point  $\mathbf{r}'$  is not in the origin.

#### APPENDIX B

The 2.5-D  $\tilde{\mathbf{G}}_A$  in a homogeneous isotropic medium is

$$\tilde{\mathbf{G}}_A = -\frac{j\mu}{4} H_0^{(2)}(k_\rho \rho) \bar{\mathbf{I}} \quad (\text{B1})$$

where  $\rho = ((x - x')^2 + (z - z')^2)^{1/2}$ ,  $k_\rho = (k^2 - k_y^2)^{1/2} = (k_x^2 + k_z^2)^{1/2}$ ,  $\mu$  is the relative permeability, and  $\bar{\mathbf{I}}$  is the unit tensor. The nine components of the 2.5-D  $\tilde{\mathbf{G}}_{EJ}$  in a homogeneous isotropic medium are

$$\begin{aligned} \tilde{G}_{EJ}^{xx} &= -\frac{\omega\mu\mu_0}{4} \cdot \left\{ H_0^{(2)}(k_\rho \rho) - \frac{k_\rho^2}{k^2} \cdot \frac{(x - x')^2}{\rho^2} H_0^{(2)}(k_\rho \rho) \right. \\ &\quad \left. - \frac{k_\rho}{k^2} \cdot \frac{(z - z')^2 - (x - x')^2}{\rho^3} \cdot H_1^{(2)}(k_\rho \rho) \right\} \end{aligned} \quad (\text{B2a})$$

$$\tilde{G}_{EJ}^{xy} = \tilde{G}_{EJ}^{yx} = -\frac{j\omega\mu\mu_0}{4} \cdot \frac{k_y \cdot k_\rho}{k^2} \cdot \frac{(x - x')}{\rho} \cdot H_1^{(2)}(k_\rho \rho) \quad (\text{B2b})$$

$$\tilde{G}_{EJ}^{xz} = \tilde{G}_{EJ}^{zx} = -\frac{\omega\mu\mu_0}{4} \cdot \frac{k_\rho^2}{k^2} \cdot \frac{(x - x') \cdot (z - z')}{\rho^2} \cdot H_2^{(2)}(k_\rho \rho) \quad (\text{B2c})$$

$$\tilde{G}_{EJ}^{yy} = -\frac{\omega\mu\mu_0}{4} \cdot \frac{k_\rho^2}{k^2} \cdot H_0^{(2)}(k_\rho \rho) \quad (\text{B2d})$$

$$\tilde{G}_{EJ}^{yz} = \tilde{G}_{EJ}^{zy} = -\frac{j\omega\mu\mu_0}{4} \cdot \frac{k_y \cdot k_\rho}{k^2} \cdot \frac{(z - z')}{\rho} \cdot H_1^{(2)}(k_\rho \rho) \quad (\text{B2e})$$

$$\begin{aligned} \tilde{G}_{EJ}^{zz} &= -\frac{\omega\mu\mu_0}{4} \cdot \left\{ H_0^{(2)}(k_\rho \rho) - \frac{k_\rho^2}{k^2} \cdot \frac{(z - z')^2}{\rho^2} H_0^{(2)}(k_\rho \rho) \right. \\ &\quad \left. - \frac{k_\rho}{k^2} \cdot \frac{(x - x')^2 - (z - z')^2}{\rho^3} \cdot H_1^{(2)}(k_\rho \rho) \right\}. \end{aligned} \quad (\text{B2f})$$

The nine components of the 2.5-D  $\tilde{\mathbf{G}}_{HJ}$  are

$$\tilde{G}_{HJ}^{xx} = \tilde{G}_{HJ}^{yy} = \tilde{G}_{HJ}^{zz} = 0 \quad (\text{B3a})$$

$$\tilde{G}_{HJ}^{xy} = -\tilde{G}_{HJ}^{yx} = -\frac{j}{4} H_1^{(2)}(k_\rho \rho) \cdot k_\rho \cdot \frac{z - z'}{\rho} \quad (\text{B3b})$$

$$\tilde{G}_{HJ}^{xz} = -\tilde{G}_{HJ}^{zx} = -\frac{k_y}{4} H_0^{(2)}(k_\rho \rho) \quad (\text{B3c})$$

$$\tilde{G}_{HJ}^{yz} = -\tilde{G}_{HJ}^{zy} = -\frac{j}{4} H_1^{(2)}(k_\rho \rho) \cdot k_\rho \cdot \frac{x - x'}{\rho}. \quad (\text{B3d})$$

Note in the above derivations, the following two identities regarding the Hankel function

$$\frac{d}{dx}[H_p(\alpha x)] = -\alpha H_{p+1}(\alpha x) + \frac{p}{x} H_p(\alpha x) \quad (\text{B4a})$$

$$H_{p-1}(\alpha x) + H_{p+1}(\alpha x) = \frac{2p}{\alpha x} H_p(\alpha x) \quad (\text{B4b})$$

are used.

## APPENDIX C

The nine components of the 2.5-D  $\tilde{\mathbf{G}}_A$  in a homogeneous uniaxial anisotropic medium are

$$\tilde{G}_A^{xx} = \tilde{G}_A^{yy} = -\frac{j\mu_{11}}{4\sqrt{\nu^h}} H_0^{(2)}(k_{\rho_h} \rho_h) \quad (\text{C1a})$$

$$\tilde{G}_A^{zz} = -\frac{j\mu_{11}\sqrt{\nu^e}}{4} H_0^{(2)}(k_{\rho_e} \rho_e) \quad (\text{C1b})$$

$$\begin{aligned} \tilde{G}_A^{zx} &= \pm \frac{\mu_{11}}{2\pi} \int_0^{+\infty} \left\{ \frac{k_x}{k_x^2 + k_y^2} \exp[-jk_z^e |z - z'|] - \frac{k_x}{k_x^2 + k_y^2} \right. \\ &\quad \left. \exp[-jk_z^h |z - z'|] \right\} \sin[k_x(x - x')] dk_x \quad (\text{C1c}) \end{aligned}$$

$$\begin{aligned} \tilde{G}_A^{zy} &= \pm \frac{j\mu_{11}}{2\pi} \int_0^{+\infty} \left\{ \frac{k_y}{k_x^2 + k_y^2} \exp[-jk_z^e |z - z'|] - \frac{k_y}{k_x^2 + k_y^2} \right. \\ &\quad \left. \exp[-jk_z^h |z - z'|] \right\} \cos[k_x(x - x')] dk_x \quad (\text{C1d}) \end{aligned}$$

$$\tilde{G}_A^{xy} = \tilde{G}_A^{xz} = \tilde{G}_A^{yx} = \tilde{G}_A^{yz} = 0 \quad (\text{C1e})$$

where

$$k_\rho = \sqrt{k^2 - k_y^2}, \quad k = \sqrt{\epsilon_{11}\mu_{11}} k_0, \quad k_{\rho_e} = \sqrt{k^2 - \nu^e k_y^2}$$

$$k_{\rho_h} = \sqrt{k^2 - \nu^h k_y^2}, \quad \rho_e = \sqrt{\frac{(x - x')^2}{\nu^e} + (z - z')^2}$$

$$\rho_h = \sqrt{\frac{(x - x')^2}{\nu^h} + (z - z')^2}, \quad k_z^e = \sqrt{k^2 - \nu^e k_x^2 - \nu^e k_y^2}$$

$$k_z^h = \sqrt{k^2 - \nu^h k_x^2 - \nu^h k_y^2}, \quad \text{and}$$

$$\nu^e = \epsilon_{11}/\epsilon_{33}, \quad \text{and} \quad \nu^h = \mu_{11}/\mu_{33}$$

are the electric and magnetic anisotropy ratios of the background medium, respectively. The nine components of the 2.5-D  $\tilde{\mathbf{G}}_{EJ}$  are

$$\begin{aligned} \tilde{G}_{EJ}^{xx} &= -\frac{1}{2\pi} \int_0^{+\infty} \left\{ \frac{k_x^2}{k_x^2 + k_y^2} \frac{k_z^e}{\omega\epsilon_{11}\epsilon_0} \exp[-jk_z^e |z - z'|] \right. \\ &\quad \left. + \frac{k_y^2}{k_x^2 + k_y^2} \frac{\omega\mu_{11}\mu_0}{k_z^h} \exp[-jk_z^h |z - z'|] \right\} \\ &\quad \times \cos[k_x(x - x')] dk_x \quad (\text{C2a}) \end{aligned}$$

$$\begin{aligned} \tilde{G}_{EJ}^{xy} = \tilde{G}_{EJ}^{yx} &= \frac{j}{2\pi} \int_0^{+\infty} \left\{ \frac{k_x k_y}{k_x^2 + k_y^2} \frac{k_z^e}{\omega\epsilon_{11}\epsilon_0} \exp[-jk_z^e |z - z'|] \right. \\ &\quad \left. - \frac{k_x k_y}{k_x^2 + k_y^2} \frac{\omega\mu_{11}\mu_0}{k_z^h} \exp[-jk_z^h |z - z'|] \right\} \\ &\quad \times \sin[k_x(x - x')] dk_x \quad (\text{C2b}) \end{aligned}$$

$$\begin{aligned} \tilde{G}_{EJ}^{xz} = \tilde{G}_{EJ}^{zx} &= -\frac{\omega\mu_{11}\mu_0}{4} \cdot \frac{k_{\rho_e}^2}{k^2} \cdot \frac{(x - x')(z - z')}{\sqrt{\nu^e} \rho_e^2} \\ &\quad \cdot H_2^{(2)}(k_{\rho_e} \rho_e) \quad (\text{C2c}) \end{aligned}$$

$$\begin{aligned} \tilde{G}_{EJ}^{yy} &= -\frac{1}{2\pi} \int_0^{+\infty} \left\{ \frac{k_y^2}{k_x^2 + k_y^2} \frac{k_z^e}{\omega\epsilon_{11}\epsilon_0} \exp[-jk_z^e |z - z'|] \right. \\ &\quad \left. + \frac{k_x^2}{k_x^2 + k_y^2} \frac{\omega\mu_{11}\mu_0}{k_z^h} \exp[-jk_z^h |z - z'|] \right\} \\ &\quad \times \cos[k_x(x - x')] dk_x \quad (\text{C2d}) \end{aligned}$$

$$\begin{aligned} \tilde{G}_{EJ}^{yz} = \tilde{G}_{EJ}^{zy} &= -\frac{j\omega\mu_{11}\mu_0}{4} \cdot \frac{\sqrt{\nu^e} k_y k_{\rho_e}}{k^2} \cdot \frac{(z - z')}{\rho_e} \\ &\quad \cdot H_1^{(2)}(k_{\rho_e} \rho_e) \quad (\text{C2e}) \end{aligned}$$

$$\begin{aligned} \tilde{G}_{EJ}^{zz} &= -\frac{\omega\mu_{11}\mu_0\sqrt{\nu^e}}{4} \\ &\quad \cdot \left\{ H_0^{(2)}(k_{\rho_e} \rho_e) - \frac{k_{\rho_e}^2}{k^2} \cdot \frac{(z - z')^2}{\rho_e^2} \right. \\ &\quad \left. \cdot H_0^{(2)}(k_{\rho_e} \rho_e) - \frac{k_{\rho_e}}{k^2} \cdot \frac{(x - x')^2/\nu^e - (z - z')^2}{\rho_e^3} \right. \\ &\quad \left. \cdot H_1^{(2)}(k_{\rho_e} \rho_e) \right\}. \quad (\text{C2f}) \end{aligned}$$

The nine components of the 2.5-D  $\tilde{\mathbf{G}}_{HJ}$  are

$$\begin{aligned} \tilde{G}_{HJ}^{xx} = -\tilde{G}_{HJ}^{yy} &= \pm \frac{-j}{2\pi} \int_0^{+\infty} \left\{ \frac{k_x k_y}{k_x^2 + k_y^2} \exp[-jk_z^e |z - z'|] - \frac{k_x k_y}{k_x^2 + k_y^2} \right. \\ &\quad \left. \exp[-jk_z^h |z - z'|] \right\} \sin[k_x(x - x')] dk_x \quad (\text{C3a}) \end{aligned}$$

$$\begin{aligned} \tilde{G}_{HJ}^{xy} &= \pm \frac{1}{2\pi} \int_0^{+\infty} \left\{ \frac{k_y^2}{k_x^2 + k_y^2} \exp[-jk_z^e |z - z'|] \right. \\ &\quad \left. + \frac{k_x^2}{k_x^2 + k_y^2} \exp[-jk_z^h |z - z'|] \right\} \\ &\quad \times \cos[k_x(x - x')] dk_x \quad (\text{C3b}) \end{aligned}$$

$$\tilde{G}_{HJ}^{xz} = -\frac{\sqrt{\nu^e} k_y}{4} H_0^{(2)}(k_{\rho_e} \rho_e) \quad (\text{C3c})$$

$$\begin{aligned} \tilde{G}_{HJ}^{yx} &= \pm \frac{-1}{2\pi} \int_0^{+\infty} \left\{ \frac{k_x^2}{k_x^2 + k_y^2} \exp[-jk_z^e |z - z'|] \right. \\ &\quad \left. + \frac{k_y^2}{k_x^2 + k_y^2} \exp[-jk_z^h |z - z'|] \right\} \\ &\quad \times \cos[k_x(x - x')] dk_x \quad (\text{C3d}) \end{aligned}$$

$$\tilde{G}_{HJ}^{yz} = -\frac{j}{4} H_1^{(2)}(k_{\rho_e} \rho_e) \cdot k_{\rho_e} \cdot \frac{x - x'}{\sqrt{\nu^e} \rho_e} \quad (C3e)$$

$$\tilde{G}_{HJ}^{zx} = \frac{\sqrt{\nu^h} k_y}{4} H_0^{(2)}(k_{\rho_h} \rho_h) \quad (C3f)$$

$$\tilde{G}_{HJ}^{zy} = \frac{j}{4} H_1^{(2)}(k_{\rho_h} \rho_h) \cdot k_{\rho_h} \cdot \frac{x - x'}{\sqrt{\nu^h} \rho_h} \quad (C3g)$$

$$\tilde{G}_{HJ}^{zz} = 0. \quad (C3h)$$

## REFERENCES

- [1] C. Yu et al., "Active microwave imaging II: 3-D system prototype and image reconstruction from experimental data," *IEEE Trans. Microw. Theory Techn.*, vol. 56, no. 4, pp. 991–1000, Apr. 2008.
- [2] T. Nagaishi, H. Ota, E. Arai, T. Hayashi, and H. Itozaki, "High Tc SQUID system for transient electromagnetic geophysical exploration," *IEEE Trans. Applied Supercond.*, vol. 15, no. 2, pp. 749–752, Jun. 2005.
- [3] H.-S. Zhao et al., "Electromagnetic scattering by artificial plasma clouds in the ionosphere," *IEEE Trans. Antennas Propag.*, vol. 68, no. 6, pp. 4810–4819, Jun. 2020.
- [4] J. Schofield, D. Daniels, and P. Hammerton, "A multiple migration and stacking algorithm designed for land mine detection," *IEEE Trans. Geosci. Remote Sens.*, vol. 52, no. 11, pp. 6983–6988, Nov. 2014.
- [5] C.-C. Chen, M. B. Higgins, K. O'Neill, and R. Detsch, "Ultrawide-bandwidth fully-polarimetric ground penetrating radar classification of subsurface unexploded ordnance," *IEEE Trans. Geosci. Remote Sens.*, vol. 39, no. 6, pp. 1221–1230, Jun. 2001.
- [6] G. Mie, "Contributions to the optics of turbid media, particularly of colloidal metal solutions," *Ann. Phys.*, vol. 330, no. 3, pp. 377–445, 1908.
- [7] W. Mundy, J. Roux, and A. Smith, "Mie scattering by spheres in an absorbing medium," *J. Opt. Soc. Amer.*, vol. 64, no. 12, pp. 1593–1597, 1974.
- [8] A. L. Aden and M. Kerker, "Scattering of electromagnetic waves from two concentric spheres," *J. Appl. Phys.*, vol. 22, no. 10, pp. 1242–1246, 1951.
- [9] Y.-L. Geng, X.-B. Wu, L.-W. Li, and B.-R. Guan, "Mie scattering by a uniaxial anisotropic sphere," *Phys. Rev. E, Stat. Phys. Plasmas Fluids Relat. Interdiscip. Top.*, vol. 70, no. 5, Nov. 2004, Art. no. 056609.
- [10] R. A. Shore and A. D. Yaghjian, "Dual-surface integral equations in electromagnetic scattering," *IEEE Trans. Antennas Propag.*, vol. 53, no. 5, pp. 1706–1709, May 2005.
- [11] S. Sharma and P. Triverio, "An accelerated surface integral equation method for the electromagnetic modeling of dielectric and lossy objects of arbitrary conductivity," *IEEE Trans. Antennas Propag.*, vol. 69, no. 9, pp. 5822–5836, Sep. 2021.
- [12] X. Millard and Q. H. Liu, "A fast volume integral equation solver for electromagnetic scattering from large inhomogeneous objects in planar layered media," *IEEE Trans. Antennas Propag.*, vol. 51, no. 9, pp. 2393–2401, Sep. 2003.
- [13] L. E. Sun, "Electromagnetic modeling of inhomogeneous and anisotropic structures by volume integral equation methods," *Waves Random Complex Media*, vol. 25, no. 4, pp. 536–548, 2015.
- [14] A. Glisson and D. Wilton, "Simple and efficient numerical methods for problems of electromagnetic radiation and scattering from surfaces," *IEEE Trans. Antennas Propag.*, vol. AP-28, no. 5, pp. 593–603, Sep. 1980.
- [15] K. Umashankar, A. Taflove, and S. Rao, "Electromagnetic scattering by arbitrary shaped three-dimensional homogeneous lossy dielectric objects," *IEEE Trans. Antennas Propag.*, vol. AP-34, no. 6, pp. 758–766, Jun. 1986.
- [16] G. K. Avdikos and H. T. Anastassiou, "Computational cost estimations and comparisons for three methods of applied electromagnetics (MoM, MAS, MMAS)," *IEEE Antennas Propag. Mag.*, vol. 47, no. 1, pp. 121–129, Feb. 2005.
- [17] T. Sarkar, E. Arvas, and S. Rao, "Application of FFT and the conjugate gradient method for the solution of electromagnetic radiation from electrically large and small conducting bodies," *IEEE Trans. Antennas Propag.*, vol. AP-34, no. 5, pp. 635–640, May 1986.
- [18] P. Zwartborn and P. M. van den Berg, "The three dimensional weak form of the conjugate gradient FFT method for solving scattering problems," *IEEE Trans. Microw. Theory Techn.*, vol. 40, no. 9, pp. 1757–1766, Sep. 1992.
- [19] H. F. Ma, J. F. Zhang, X. Chen, Q. Cheng, and T. J. Cui, "CG-FFT algorithm for three-dimensional inhomogeneous and biaxial metamaterials," *Waves Random Complex Media*, vol. 19, no. 1, pp. 49–64, Feb. 2009.
- [20] H. Gan and W. C. Chew, "A discrete BCG-FFT algorithm for solving 3D inhomogeneous scatterer problems," *J. Electromagn. Waves Appl.*, vol. 9, no. 10, pp. 1339–1357, Jan. 1995.
- [21] Z. Q. Zhang and Q. H. Liu, "Three-dimensional weak-form conjugate-and biconjugate-gradient FFT methods for volume integral equations," *Microw. Opt. Technol. Lett.*, vol. 29, no. 5, pp. 350–356, Jun. 2001.
- [22] H. A. van der Vorst, "Bi-CGSTAB: A fast and smoothly converging variant of bi-CG for the solution of nonsymmetric linear systems," *SIAM J. Sci. Stat. Comput.*, vol. 13, no. 2, pp. 631–644, Mar. 1992.
- [23] X. Min Xu and Q. H. Liu, "The BCGS-FFT method for electromagnetic scattering from inhomogeneous objects in a planarly layered medium," *IEEE Antennas Wireless Propag. Lett.*, vol. 1, pp. 77–80, 2002.
- [24] V. Rokhlin, "Rapid solution of integral equations of scattering theory in two dimensions," *J. Comput. Phys.*, vol. 86, no. 2, pp. 414–439, 1990.
- [25] N. Engheta, W. D. Murphy, V. Rokhlin, and M. S. Vassiliou, "The fast multipole method (FMM) for electromagnetic scattering problems," *IEEE Trans. Antennas Propag.*, vol. 40, no. 6, pp. 634–641, Jun. 1992.
- [26] J. Song, C.-C. Lu, and W. C. Chew, "Multilevel fast multipole algorithm for electromagnetic scattering by large complex objects," *IEEE Trans. Antennas Propag.*, vol. 45, no. 10, pp. 1488–1493, Oct. 1997.
- [27] E. Bleszynski, M. Bleszynski, and T. Jaroszewicz, "AIM: Adaptive integral method for solving large-scale electromagnetic scattering and radiation problems," *Radio Sci.*, vol. 31, no. 5, pp. 1225–1251, Sep. 1996.
- [28] J. R. Phillips and J. K. White, "A precorrected-FFT method for electrostatic analysis of complicated 3-D structures," *IEEE Trans. Comput.-Aided Design Integr. Circuits Syst.*, vol. 16, no. 10, pp. 1059–1072, Oct. 1997.
- [29] X.-C. Nie, L.-W. Li, and N. Yuan, "Precorrected-FFT algorithm for solving combined field integral equations in electromagnetic scattering," *J. Electromagn. Waves Appl.*, vol. 16, no. 8, pp. 1171–1187, Jan. 2002.
- [30] T. Lan, N. Liu, Y. Liu, F. Han, and Q. H. Liu, "2-D electromagnetic scattering and inverse scattering from magnetodielectric objects based on integral equation method," *IEEE Trans. Antennas Propag.*, vol. 67, no. 2, pp. 1346–1351, Feb. 2019.
- [31] Z. Yu, W. Zhang, and Q. H. Liu, "The mixed-order BCGS-FFT method for the scattering of three-dimensional inhomogeneous anisotropic magnetodielectric objects," *IEEE Trans. Antennas Propag.*, vol. 63, no. 12, pp. 5709–5717, Dec. 2015.
- [32] J. Zhuo, F. Han, L. Ye, Z. Yu, and Q. H. Liu, "Simulation of electromagnetic scattering of 3-D inhomogeneous biaxial anisotropic magnetodielectric objects embedded in uniaxial anisotropic media by the mixed-order BCGS-FFT method," *IEEE Trans. Microw. Theory Techn.*, vol. 66, no. 8, pp. 3745–3755, Aug. 2018.
- [33] F. Han, J. Zhuo, N. Liu, Y. Liu, H. Liu, and Q. H. Liu, "Fast solution of electromagnetic scattering for 3-D inhomogeneous anisotropic objects embedded in layered uniaxial media by the BCGS-FFT method," *IEEE Trans. Antennas Propag.*, vol. 67, no. 3, pp. 1748–1759, Mar. 2019.
- [34] J. Wang, J. Li, Y. Chen, F. Han, and Q. H. Liu, "Simulation of 3-D electromagnetic scattering and inverse scattering by arbitrary anisotropic dielectric objects embedded in layered arbitrary anisotropic media," *IEEE Trans. Antennas Propag.*, vol. 68, no. 8, pp. 6473–6478, Aug. 2020.
- [35] S. B. Sayed et al., "A butterfly-accelerated volume integral equation solver for broad permittivity and large-scale electromagnetic analysis," *IEEE Trans. Antennas Propag.*, vol. 70, no. 5, pp. 3549–3559, May 2022.
- [36] Y.-N. Liu, X.-M. Pan, and X.-Q. Sheng, "Fast direct solution of 3-D volume integral equations by skeletonization for dynamic electromagnetic wave problems," *Int. J. Numer. Model. Electron. Netw. Devices Fields*, vol. 33, no. 2, p. 2667, Mar. 2020.
- [37] K. Key and J. Oval, "A parallel goal-oriented adaptive finite element method for 2.5-D electromagnetic modelling," *Geophys. J. Int.*, vol. 186, no. 1, pp. 137–154, Jul. 2011.
- [38] F. Sugeng, A. Raiche, and L. Rijo, "Comparing the time-domain EM response of 2-D and elongated 3-D conductors excited by a rectangular loop source," *J. Geomagnetism Geoelectricity*, vol. 45, no. 9, pp. 873–885, 1993.

- [39] Z. Jiang, S. Liu, and R. Malekian, "Analysis of a whole-space transient electromagnetic field in 2.5-dimensional FDTD geoelectric modeling," *IEEE Access*, vol. 5, pp. 18707–18714, 2017.
- [40] A. Abubakar, P. M. van Den Berg, and T. M. Habashy, "An integral equation approach for 2.5-dimensional forward and inverse electromagnetic scattering," *Geophys. J. Int.*, vol. 165, no. 3, pp. 744–762, Jun. 2006.
- [41] S. Van den Bulcke and A. Franchois, "A full-wave 2.5D volume integral equation solver for 3D millimeter-wave scattering by large inhomogeneous 2D objects," *IEEE Trans. Antennas Propag.*, vol. 57, no. 2, pp. 535–545, Feb. 2009.
- [42] S. Van den Bulcke, L. Zhang, A. Franchois, J. M. Geffrin, and J. Stiens, "Plane wave and Gaussian beam scattering by long dielectric cylinders: 2.5D simulations versus measurements," *Int. J. Infr. Millim. Waves*, vol. 29, no. 11, pp. 1038–1047, Aug. 2008.
- [43] E. Babolian, M. MasjedJamei, and M. R. Eslahchi, "On numerical improvement of Gauss-Legendre quadrature rules," *Appl. Math. Comput.*, vol. 160, no. 3, pp. 779–789, Jan. 2005.
- [44] K. A. Michalski and J. R. Mosig, "Multilayered media Green's functions in integral equation formulations," *IEEE Trans. Antennas Propag.*, vol. 45, no. 3, pp. 508–519, Mar. 1997.
- [45] Z. Wu, Y. Fan, J. Wang, R. Zhang, and Q. H. Liu, "Application of 2.5-D finite difference method in logging-while-drilling electromagnetic measurements for complex scenarios," *IEEE Geosci. Remote Sens. Lett.*, vol. 17, no. 4, pp. 577–581, Apr. 2020.
- [46] F. Han, J. Zhuo, S. Lu, J. Wang, and Q. H. Liu, "Explicit semianalytical expressions of sensitivity matrices for the reconstruction of 1-D planarly layered TI media illuminated by 3-D sources," *IEEE Trans. Antennas Propag.*, vol. 70, no. 2, pp. 1547–1552, Feb. 2022.
- [47] W. C. Chew, *Waves and Fields in Inhomogeneous Media*. New York, NY, USA: IEEE, 1995, ch. 2, p. 59.
- [48] J. Li, J. Zhuo, Y. Chen, F. Han, and Q. H. Liu, "Retrieval of composite model parameters for 3-D microwave imaging of biaxial objects by BCGS-FFT and PSO," *IEEE Trans. Microw. Theory Techn.*, vol. 68, no. 5, pp. 1896–1907, May 2020.



**Feng Han** (Senior Member, IEEE) received the B.S. degree in electronic science from Beijing Normal University, Beijing, China, in 2003, the M.S. degree in geophysics from Peking University, Beijing, in 2006, and the Ph.D. degree in electrical engineering from Duke University, Durham, NC, USA, in 2011.

From 2011 to 2015, he was a Software Engineer with Wavenovation, Inc., Xiamen, China. In July 2015, he joined the Institute of Electromagnetics and Acoustics, Xiamen University, Xiamen, as an Assistant Professor, and was promoted to an Associate Professor there in 2020. In October 2023, he joined the School of Computing and Information Technology, Great Bay University, Guangdong, China, as an Associate Professor. He has published over 60 articles in refereed journals. His research interests include electromagnetic scattering and inverse scattering in complex media, multiparametric and multidimensional hybrid electromagnetic full-wave inversion, fast electromagnetic full-wave inversion based on scientific machine learning, configuration of the antenna array for electromagnetic inverse problems, and geophysical electromagnetic exploration and inversion.



**Kemeng Tao** received the B.E. degree in electronic information engineering from Xiangtan University, Xiangtan, China, in 2020, and the M.S. degree in electromagnetic field and microwave technology from Xiamen University, Xiamen, China, in 2024.

She is currently a Research Assistant with the School of Computing and Information Technology, Great Bay University, Guangdong, China. Her research interests include electromagnetic scattering and inverse scattering in complex media and antenna array configuration for electromagnetic full-wave inversion.



**Sijia Ma** received the B.S. degree in electronic information science and technologies from Shaanxi Normal University, Xi'an, China, in 2021, and the M.S. degree in electromagnetic field and microwave technology from Xiamen University, Xiamen, China, in 2024.

She is currently a Research Assistant with the School of Computing and Information Technology, Great Bay University, Guangdong, China. Her research interests include electromagnetic scattering and inverse scattering in complex media and antenna

array configuration for electromagnetic full-wave inversion.



and inverse scattering anisotropic targets.

**Jiawen Li** received the B.S. degree in electronic science and technology from Wuhan University of Technology of China, Wuhan, China, in 2011, and the Ph.D. degree in electromagnetic field and microwave technology from Xiamen University, Xiamen, China, in 2023.

Since August 2023, he has been with Guangxi Normal University, Guilin, China, where he is currently an Assistant Professor with the School of Electronic and Information Engineering. His research interests include electromagnetic scattering in complex media and the full-wave inversion of

929  
930  
931  
932  
933  
934  
935  
936  
937  
938  
939  
940  
941  
942  
943  
944  
945  
946  
947  
948  
949  
950  
951  
952  
953  
954  
955  
956  
957  
958  
959  
960  
961  
962  
963  
964  
965  
966  
967  
968  
969  
970  
971  
972  
973  
974  
975  
976  
977  
978  
979  
980  
981  
982  
983  
984  
985  
986  
987  
988  
989  
990  
991  
992  
993  
994  
995  
996  
997  
998  
999  
1000  
1001  
1002  
1003  
1004  
1005  
1006  
1007  
1008  
1009  
1010  
1011  
1012  
1013  
1014  
1015  
1016  
1017  
1018  
1019  
1020